SmokeBot

Mobile Robots with Novel Environmental Sensors for Inspection of Disaster Sites with Low Visibility

Project start: January 1, 2015

Duration: 3.5 years

Deliverable 3.1

Technical Description for Correction of Radiation Disturbances

Due date: month 9 (September 2015)

Lead beneficiary: LUH

Dissemination Level: PUBLIC

Main Authors:

Björn Zeise (LUH)

Version History:

0.1: Initial version, BZ, Jul 2015

0.2: Added reflection handling and smoke experiments, BZ, Aug 2015

0.3: Final version, BZ, Sep 2015

Contents

Abstract

This document is a technical report within the scope of the Horizon 2020 project SmokeBot. SmokeBot's objective is to improve the application of mobile robots in disaster scenarios with low visibility conditions. A key element of the project is to develop perception algorithms that support the cooperation of humans and machines in search and rescue missions. This is done with the aid of a novel, multimodal sensor unit, which combines radar, gas, thermal and traditional vision sensors.

This report summarizes the results of Task 3.1 ("Handling of Thermal-Radiation Disturbances – Reflections and Gas Radiation"). Task 3.1 is part of Work Package 3 ("Thermal Imaging"), which aims at combining temperature data and 3D structures in order to create partial 3D surface temperature maps. The objective of Task 3.1 in particular is to perform a detection and correction of measurement disturbances in thermal images. This report includes theory and experimental investigation of thermal radiation disturbances regarding images taken by a thermal imaging camera system.

1. Introduction

In today's search and rescue applications, thermal imaging cameras are widely used for tasks such as human detection [1] [2], exploration of forest/smoldering fires [3] [4] and detection of potential hazards [5]. In SmokeBot, thermal imaging cameras shall especially be used for the latter task.

Although thermography has proved to be very useful in disaster scenarios, the interpretation of thermal images is a challenge for humans and especially for robots. This arises from the fact that thermography depends on environmental influences/conditions in many ways. Only to name a few, there are dependencies on material category, viewing angle, surface character, surrounding mediums, etc. The disturbances/misinterpretations considered in this report originate from three different sources: from unknown emissivity values, from thermal reflections and from the influence of smoke between the thermal imaging camera and the regarded object.

The considerations in this report apply to experiments performed with a thermal imaging camera working in the long-wave infrared spectrum ($7.5\ \mu m$ to $14\ \mu m$). Note that may not all presented results are applicable to other kinds of thermal imaging systems.

The report is organized as follows:

- First, we recap the basics on thermography in order to show some typical examples for misinterpretations in thermal images. On the basis of these examples, we provide a brief overview on related work.
- Afterwards, we explain how to exploit the camera's viewing angle to estimate unknown surface emissivities and real temperatures.
- Then, we present an approach to detection and removal of thermal reflections.
- Afterwards, we investigate the influence of smoke (as the medium between camera and regarded surface) on thermal images.
- In the end, we conclude the report with a summary.

2. Challenges in Thermal Imaging

In order to understand the origin of misinterpretations in thermal images, a basic knowledge of thermography is needed. After explaining the fundamentals, we give practical examples on misinterpretations in thermal images.

2.1 Thermography Basics

The underlying principle of thermography is radiation heat transfer, which is – besides conduction and convection – one of the three types of heat transfer. Each object/body whose temperature is above absolute zero ($0\ K$) emits electromagnetic radiation. According to the third law of thermodynamics, this holds for each existing body, because absolute zero cannot be obtained by any body.

The amount of radiation a body emits generally depends on many factors. To ease calculation with radiation intensities, an ideal physical model called *black body* is used. A black body always absorbs the whole amount of incoming radiation energy simultaneously emitting it again. The spectral black body intensity I^{bb} can be expressed using Planck's law:

$$I^{bb}(\lambda, T) = \frac{2\pi hc^2}{\lambda^5(\exp\left(\frac{hc}{\lambda kT}\right) - 1)}. \quad (1)$$

It only depends on the radiation's wavelength λ and the body's temperature T. The known constants in Equation (1) are Planck's constant h, Boltzmann constant k and the speed of light c.

As stated before, Planck's law can only be used to describe ideal (non-existing) bodies. To describe the emitted radiation of real bodies, a body/surface property called *emissivity* was introduced. The emissivity ε is the ratio between the emitted spectral intensity of a real body I^{real} and the emitted spectral intensity of a black body I^{bb} that has the same temperature:

$$\varepsilon(\lambda, T, \Theta, \dots) = \frac{I^{real}(\lambda, T, \Theta, \dots)}{I^{bb}(\lambda, T)}. \quad (2)$$

Using Equation (2) it is possible to shift all the (unknown) radiation intensity dependencies (camera's viewing angle, surface roughness, type of surface material etc.) to the emissivity. This is an important fact regarding the measurement principle of thermal imaging cameras. They measure the radiation intensity coming from a regarded surface. That means that the measured intensity does not only correspond to the radiation intensity emitted by the regarded surface, but also to radiation parts of the surroundings (reflections) and the atmosphere between camera and surface. This can be expressed as

$$I_{sum} = I_{obj} + I_{amb} + I_{atm}, \quad (3)$$

where I_{obj}, I_{amb} and I_{atm} stand for the radiation intensities emitted by the object itself, the ambience around the object and the atmosphere between camera and object. Combining

Equations (2) and (3) and introducing the *atmospheric transmittance* τ, the measured radiation intensity of a regarded surface point is calculated as:

$$I_{sum} = \tau\varepsilon I_{obj}^{bb} + \tau(1-\varepsilon)I_{amb}^{bb} + (1-\tau)I_{atm}^{bb}. \quad (4)$$

Notice that the partial radiation intensities in Equation (4) are calculated using Equation (1).

2.2 Misinterpretation of Thermal Images

The misinterpretations in thermal images investigated in Task 3.1 arise from the relation introduced in Equations (3) and (4). The major influence on these misinterpretations comes from the emissivity. As shown in the equations, an emissivity close to unity eliminates the reflected radiation intensity part, whereas an emissivity close to zero makes it difficult to infer the real object temperature. Another influencing factor is the atmospheric radiation part, i.e. the radiation that is emitted respectively absorbed by the medium between the camera and the regarded surface. In the following there are some typical examples for misinterpretations in thermal images that are caused by the mentioned reasons.

The main challenge in thermography is the unknown emissivity when looking at objects. In professional thermography (e.g. in building diagnostics, condition monitoring, etc.), unknown emissivities are often bypassed using a high-emissivity coating (e.g. high-emissivity paint). Applying this coating to regarded surface areas diminishes misinterpretations caused by low emissivity and simultaneously avoids reflections. In Figure 1, this procedure is depicted. The whole thermal image is interpreted using an emissivity of $\varepsilon = 1$. In the front, there is a heated, polished aluminum plate (low emissivity) with a stripe of duct tape (high emissivity) on it. Although the aluminum plate and the duct tape have roughly the same temperature on the entire surface (about 330 K), their temperatures are interpreted differently. Due to the previously discussed relations between the true object temperature and the actually measured intensity, the

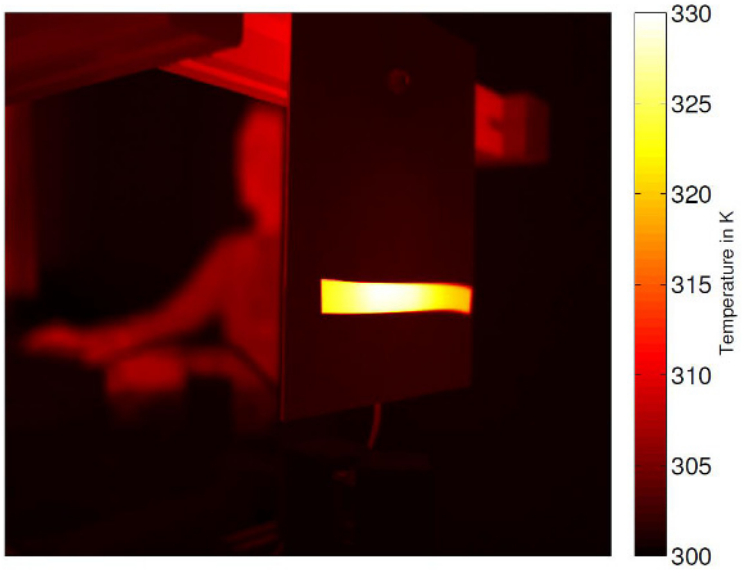

Figure 1: Example for misinterpretation in thermal image caused by unknown emissivity. See the text for a detailed explanation.

Figure 2: Exemplary thermal reflection of a human hand on a polished aluminum plate (left). For comprehension, the scene is also shown as a RGB image (right).

temperature of the blank metal surface is interpreted much lower than the temperature of the dielectric duct tape.

Emissivity and temperature estimation was investigated by numerous researchers in the past. A common technique to estimate emissivity is the dual-wavelength (*two-color*) method, where two sensors working in different wavelength ranges are used. In [6], a system of nonlinear equations is created with the help of two thermal imaging cameras. Using model equations as presented in [7], emissivity and temperature can be estimated simultaneously. A practical approach to measurement of brake disc surface temperature was presented in [8]. The authors developed a two-color pyrometer and compared their evaluation results to a commercially available product.

Another effect of low-emissivity surfaces are reflections. As described in Equation (4) a low emissivity is always associated with high reflectivity. In Figure 2, a typical reflection on a polished aluminum surface is depicted. In general, thermal reflections behave similar compared to reflections in the visible spectrum, but not all reflective surfaces in the visible spectrum also reflect in the thermal spectrum. As shown in the figure, the reflection on the aluminum plate in the thermal image is more intensive than the reflection in the RGB image. Just the opposite could be seen on an uncoated window glass that reflects well in the visible spectrum, but barely in the thermal image.

Thermal reflections can be handled in multiple ways. Besides the usage of high-emissivity coatings that were mentioned earlier, a typical approach in practical thermography is to avoid thermal reflections by choosing an appropriate point of view. For outdoor applications it can be useful to position the camera in such a way that the sky is reflected. The authors of [9] did this and took image sequences while the clouds in the sky were moving. Observing the object this way for several minutes, they were able to determine the moments in time when the reflection was minimized (because of clouds being in line of sight) in order to measure the actual object temperature.

Another approach to reflection handling is the suppression of reflections with the help of an infrared polarizing filter in front of the camera. This was presented in [10] and showed partially good result. Limitations of the method are the need to purchase an expensive infrared polarizing

filter (commonly made of germanium) as well as the strict spatial setup between camera, filter and regarded surface that is needed for successful suppression of reflections.

Software-based approaches to reflection handling are particularly known for RGB images, but can be transferred to thermal images as well. Besides the other approaches, software-based reflection handling can usually also be applied on autonomous systems working indoor. There are various methods either using one individual input image [11] [12] or multiple ones [13] [14] [15]. The general principle of all these methods is to extract several layers from the image (e.g. background and foreground layer). This relies on the assumption that the input image is a linear superposition of multiple images/layers (i.e. object layer and one or more reflection layers). The detailed possibilities to detect and remove reflections from images are discussed in Section 4.

The third misinterpretation investigated in Task 3.1 arises from smoke between the camera and the regarded surface. In non-disaster applications, the most probable transmission medium is air. Although air is mostly transparent in the thermal infrared spectrum, smoke, fog and dust can have influence on the thermal image. Research considering navigation sensors in fire smoke environments has been done by [16]. The authors found that dense, low-temperature smoke as well as light, high-temperature smoke do not affect the accuracy of thermal imaging cameras. Additionally, it was shown that a thermal stereo vision system performs well in these smoke scenarios. Similar results were reported in [17], where the authors evaluated the effect of water sprays on fire fighter thermal imagers. As both of the works show, maintaining accuracy does not mean that there is no change in the measured radiation intensity.

The different characteristics of radiation intensity for fire, smoke, reflections and other objects have been exploited in [18] in order to classify regions of interest in a thermal image. The authors used a supervised machine learning approach in combination with first and second order texture features (mean, variance, entropy and inverse difference moment) to identify the regions. The presented method works best for smoke regions.

3. Unknown Surface Emissivity

As explained in the previous sections, unknown emissivity values can lead to misinterpretations of thermal images. Emissivity depends on several quantities, such as viewing angle, surface roughness or surface material. In our research on this topic, we focused on the viewing angle dependency in order to identify the material class of the regarded surface. After material classification, emissivity and temperature are estimated and corrected.

Regarding opaque bodies/surfaces, there is an essential difference between metals and dielectrics in their emissivity characteristics. This difference comes mostly from the viewing angle dependency of the emissivity.

In Figure 3, the viewing angle (angle between the surface normal of the regarded surface and the camera's optical axis) is depicted. Depending on this angle the emissivity of metals and dielectrics behave differently. This circumstance is shown in Figure 4. While for metals the emissivity is constant low for viewing angles between 0 ° and 60 °, it then grows to a maximum just before reaching its minimum at 90 °. For ideal dielectrics, the emissivity has a constant high value at viewing angles between 0 ° and 50 °. At higher angles, it monotonically decreases to zero.

During our investigation (see also Appendix A) we exploited the described dependency to first identify the surface material class, i.e. to distinguish between metals and dielectrics, and then to calculate a corrected emissivity/temperature value for each pixel in the image. We did this by taking several thermal images from different points of view.

During the experiments described below, we made the following assumptions:

1) The regarded surfaces are assumed to be *gray*, which means that their emissivity does not depend on wavelength [7, p. 65].
2) The surface is assumed to be optically smooth, which means that roughness, texture and surface imperfection have to be smaller than the wavelength of the incident radiation [7, p. 88].

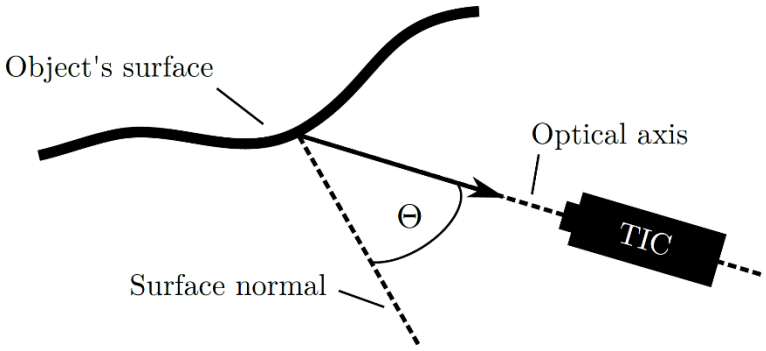

Figure 3: Illustration of the viewing angle Θ, which is the angle between the surface normal and the camera's optical axis.

3) The viewing angle Θ is known for every individual measurement.
4) The emissivity's dependency on the surface temperature is assumed to be weak.
5) The transmittance is assumed to be unity, because the distance between the camera and the surface is small and the transmission medium is air.
6) The surface and ambient temperatures are unknown but constant.
7) The surface temperature is higher than the ambient temperature.

3.1 Material Classification

In order to do a basic material classification, we used a semi-empirical adaption of Planck's law as presented in [19] to calculate the camera detector signal S:

$$S = \frac{R}{\exp\left(\frac{B}{T}\right) - F}. \tag{5}$$

The camera-specific parameters R, B and F in Equation (5) are usually determined during factory calibration and can be obtained by the camera manufacturer. The detector signal S is the camera output signal.

Combining Equations (4) and (5) and considering the assumptions made in the previous section leads to the following expression:

$$S = \varepsilon(\Theta)\left(\frac{R}{\exp\left(\frac{B}{T_{obj}}\right) - F} - \frac{R}{\exp\left(\frac{B}{T_{amb}}\right) - F}\right) + \frac{R}{\exp\left(\frac{B}{T_{amb}}\right) - F}. \tag{6}$$

Equation (6) shows the detector signal's linear dependency on the emissivity. That means that considering only the raw sensor signal, it is possible to draw qualitative conclusions about the emissivity.

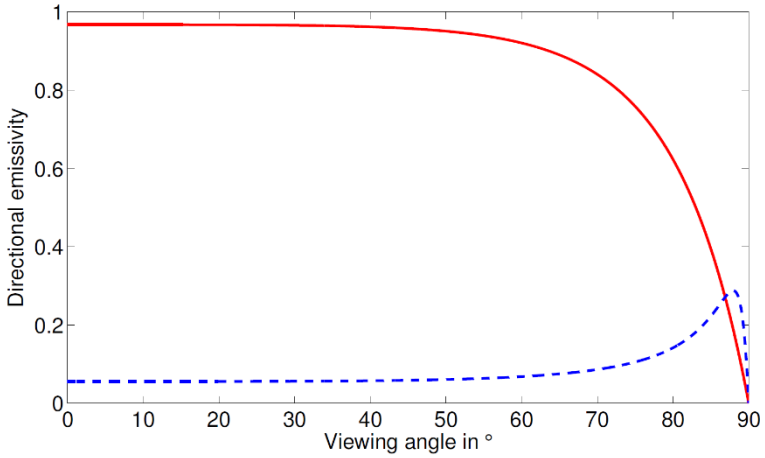

Figure 4: Exemplary comparison of the different emissivity characteristics of metals (dashed line) and dielectrics (solid line) at varying viewing angles.

In our approach, we use this to determine whether the regarded surface point shows metal or dielectric characteristic. Calculating the sum of differences between consecutive (in the sense of a growing viewing angle) thermal images, dielectric pixels reported a negative value (due to the emissivity's angular dependency shown in Figure 4). The same calculation for metal pixels instead resulted in a positive value.

Notice that – in order to make sure that corresponding surface points are used for calculation – the knowledge of the regarded 3D structure is demanded for our approach.

3.2 Emissivity/Temperature Estimation and Image Correction

To estimate emissivity and temperature of a surface point, we use a system of nonlinear equations. A similar approach was presented in [6], where emissivity and temperature were estimated using two thermal imaging cameras working in two different wavelength ranges. The system of equations consists of expressions in the form of:

$$S_i = \varepsilon(\Theta_i)\left(\frac{R}{\exp\left(\frac{B}{T_{obj}}\right) - F}\right) + \left(1 - \varepsilon(\Theta_i)\right)\frac{R}{\exp\left(\frac{B}{T_{amb}}\right) - F}, \tag{7}$$

where S_i is the detector signal of the measurement (pixel value) taken at viewing angle Θ_i. The emissivity ε can be replaced by model equations as presented in [7]. These equations only depend on the viewing angle and two optical material constants (refractive index n and extinction coefficient k). Putting the model equations in Equation (7) allows us to solve the following least square minimization problem:

$$\min_{\boldsymbol{p}} f(\boldsymbol{p}) = \min_{\boldsymbol{p}} \sum_{i=1}^{z} \left(S_i^m - S_i^c(\boldsymbol{p})\right)^2. \tag{8}$$

In Equation (8), $f(\boldsymbol{p})$ is the objective function, whose set of parameters $\boldsymbol{p} = \{n, k, T_{obj}, T_{amb}\}$ shall be optimized. The signals S_i^m and S_i^c are measured/calculated pixel values at different viewing angles, where z is the number of thermal images taken into account.

3.3 Evaluation

We evaluated the presented approach in three ways. First, we only considered one individual pixel (the pixel in the camera's optical axis) of either metal or dielectric characteristic. After that, we considered a line of pixels of both metal and dielectric characteristics. The final evaluation was performed on a mobile robot using a temperature mapping algorithm. In the first two experiments, we measured the viewing angles manually using a protractor. In the last experiment, the mapping algorithm provided the angle information. The estimated temperatures were evaluated using a surface thermometer.

The experimental setup consists of an aluminum plate heated by a $22\ W$ heatpad. The thermal imaging camera is mounted on an aluminum profile that can be rotated around the vertical axis

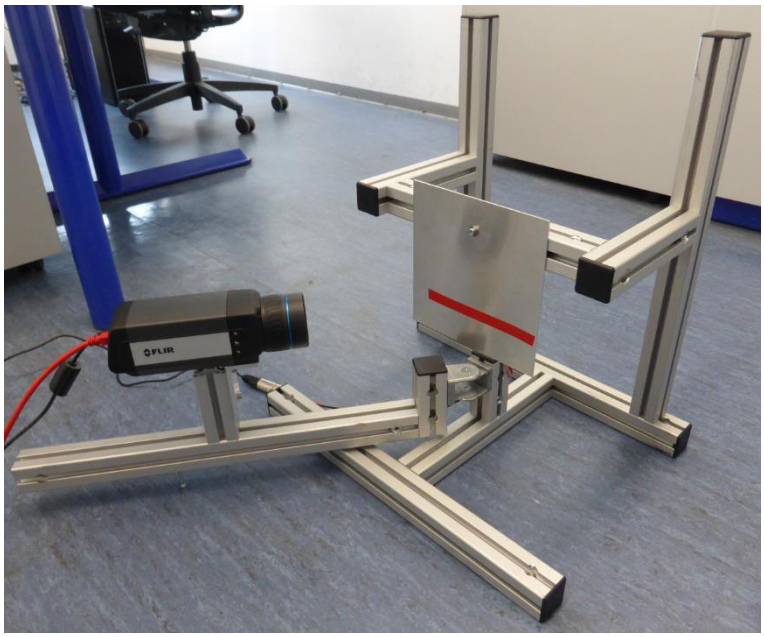

Figure 5: Experimental setup for the single point and line evaluation.

centered at the middle of the heated plate. This way, the camera can be rotated manually between viewing angles of 0 ° and 90 °. The setup is depicted in Figure 5. To ensure that the prior made assumptions are satisfied, the camera is mounted as close as possible (approx. 15 cm) in front of the heated plate. In order to simulate a constant ambient temperature, we prevent any unwanted reflections by putting a cardboard in the reflection's line of sight. By doing this, only the constant temperature of the cardboard can be "seen" as a reflection.

The thermal imaging camera used during our research is a FLIR A655sc. It has a spatial resolution of 640 x 480 pixels and works in the spectral range between 7.5 μm to 14 μm. Additionally, it has a field of view of 45 ° x 34 ° and a thermal sensitivity of 30 mK. The following calculations were performed using the Matlab environment. For optimization, the Nelder-Mead Simplex Method [20] is used.

Figure 6 shows the resulting detector signal graph using the estimated parameters. For comparison, the measured intensity values are marked along the graph. The graph shows good

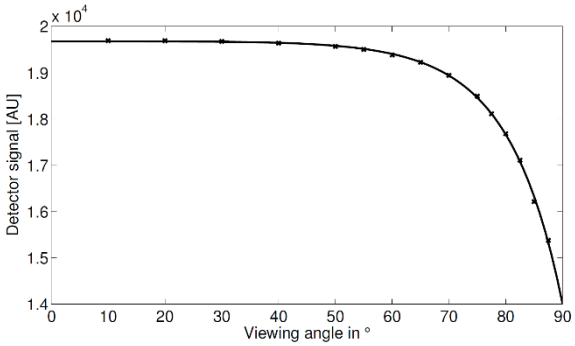

Figure 6: Dielectric surface point: detector signal graph based on estimated parameters n, T_{obj} and T_{amb} (solid line); points (x) mark the measured values.

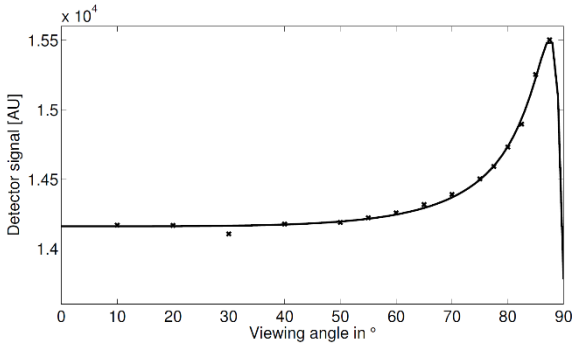

Figure 7: Metal surface point: detector signal graph based on estimated parameters n, k, T_{obj} and T_{amb} (solid line); points (x) mark the measured values.

Table 1: Evaluation results regarding individual surface points.

	Dielectric surface point	Metal surface point
T_{obj_meter}	328.55 K	329.25 K
T_{obj}	330.02 K	332.29 K
$Err(T_{obj})$	1.47 K	3.04 K
T_{amb_meter}	299.55 K	298.35 K
T_{amb}	299.31 K	297.94 K
$Err(T_{amb})$	-0.24 K	-0.41 K
n	1.4349	8.3727
k	-	22.1182

correspondence to the individual pixel values, which is also expressed in the estimated temperature values as seen in Table 1. There are only small absolute temperature errors $Err(T_{obj})$ and $Err(T_{amb})$ with respect to the measurements taken with the calibrated thermometer.

Figure 7 shows the results of an analog experiment for a metal surface point. Similar to the dielectric case, the graph shows good correspondence. There is only one bigger misalignment at a viewing angle of 30 °.

The second evaluation was performed considering a line of points on the surface. While in the previous single point evaluation the emissivity characteristic (i.e. the information, whether the regarded point has dielectric or metal characteristic) has been determined manually, in this

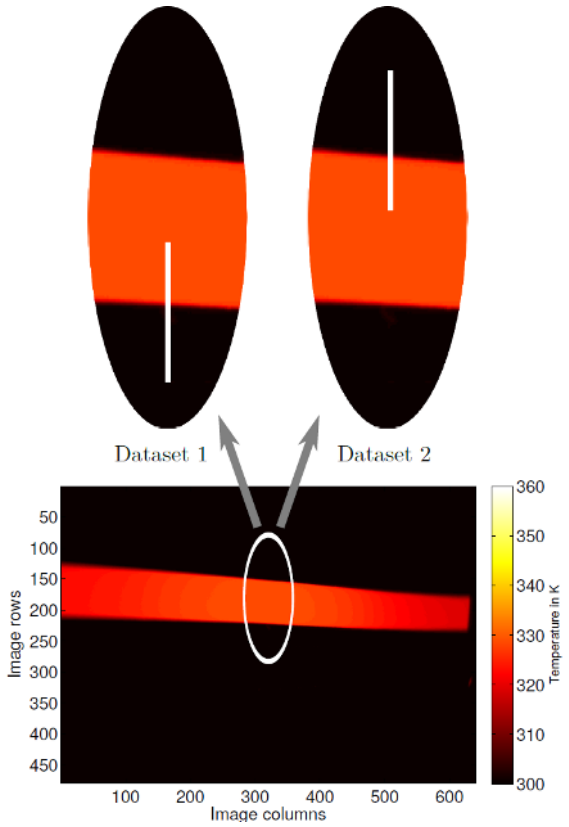

Figure 8: Illustration of the surface points that were considered during the experiment. The bottom picture shows an exemplary thermal image interpreted with an emissivity $\varepsilon = 1$. The white lines in the image sections on the top depict the regarded pixels for two different datasets.

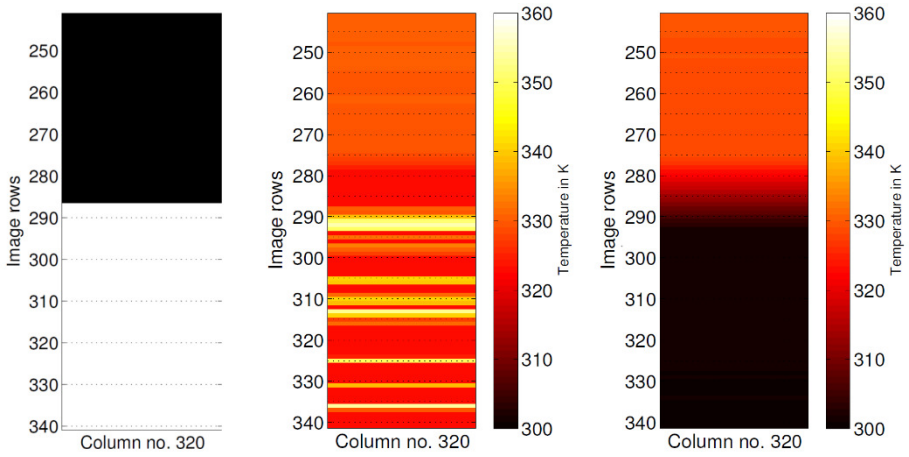

Figure 9: Evaluation results for dataset 1. All pictures represent a vertical line of points/pixels on the surface. Partial result of material classification can be seen in the figure on the left (black areas: dielectric surface, white areas: metal surface). The figure in the middle shows the corrected thermal image after applying material classification and temperature estimation. For comparison, an incorrectly interpreted image assuming an emissivity of $\varepsilon = 1$ is depicted on the right.

experiment it was provided by the material classification algorithm. Figure 8 illustrates, which surface points were considered during this experiment.

The evaluation was performed with two different datasets (each 15 images taken from varying points of view). Figure 9 shows the evaluation results for the first dataset. It can be seen, that an overall improvement in the temperature interpretation was achieved compared to the source image. The results for the second dataset (Figure 10) also show an improvement towards the initial image. Detailed measurement values are given in Table 2. Although the estimation step produced some outliers (indicated by the minimum and maximum estimated values in the table), the estimated mean value over all regarded pixels has a small absolute error with respect to the measurement taken by the thermometer.

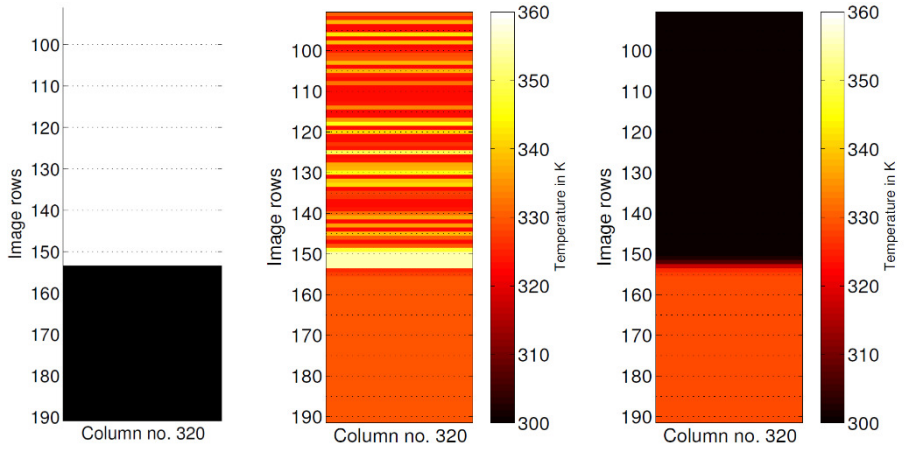

Figure 10: Evaluation results for dataset 2. All pictures represent a vertical line of points/pixels on the surface. Partial result of material classification can be seen in the figure on the left (black areas: dielectric surface, white areas: metal surface). The figure in the middle shows the corrected thermal image after applying material classification and temperature estimation. For comparison, an incorrectly interpreted image assuming an emissivity of $\varepsilon = 1$ is depicted on the right.

Table 2: Evaluation results regarding a line of points on the surface.

		Dataset 1	Dataset 2
Dielectric points	T_{obj_meter}	327.25 K	327.65 K
	T_{obj_min}	322.53 K	325.76 K
	T_{obj_max}	330.37 K	329.95 K
	T_{obj_mean}	328.39 K	329.41 K
	$Err(T_{obj})$	1.14 K	1.76 K
Metal points	T_{obj_meter}	328.35 K	328.85 K
	T_{obj_min}	322.53 K	322.53 K
	T_{obj_max}	354.62 K	354.62 K
	T_{obj_mean}	329.48 K	331.15 K
	$Err(T_{obj})$	1.13 K	2.30 K

Beside the evaluations using a fixed experimental setup, we equipped a mobile robot in order to make the first move towards transferring our approach to the real use case. The mobile robot we used is a Pioneer 2. Combining the thermal imaging camera with a Microsoft Kinect v2 time-of-flight depth sensor, we performed a simple temperature mapping. That means that the 2D thermal images were projected on the 3D structure detected by the depth sensor. This allowed us to calculate the viewing angle directly out of the spatial correlation between camera and surface. The viewing angle information was then fed into the estimation algorithm to perform the evaluation of an individual dielectric surface point (as explained in the beginning of this section). Unfortunately, we were not able to consider metal surface points, because the depth sensor could not detect these. The experimental setup used during the mobile robot evaluation is shown in Figure 11.

The results of the mobile robot evaluation are not as convincing as the results of the previous experiments. Although the estimated signal detector graph aligns well with the measured pixel values (see Figure 12), there are large absolute temperature errors of $Err(T_{obj}) = 2.95\ K$ and

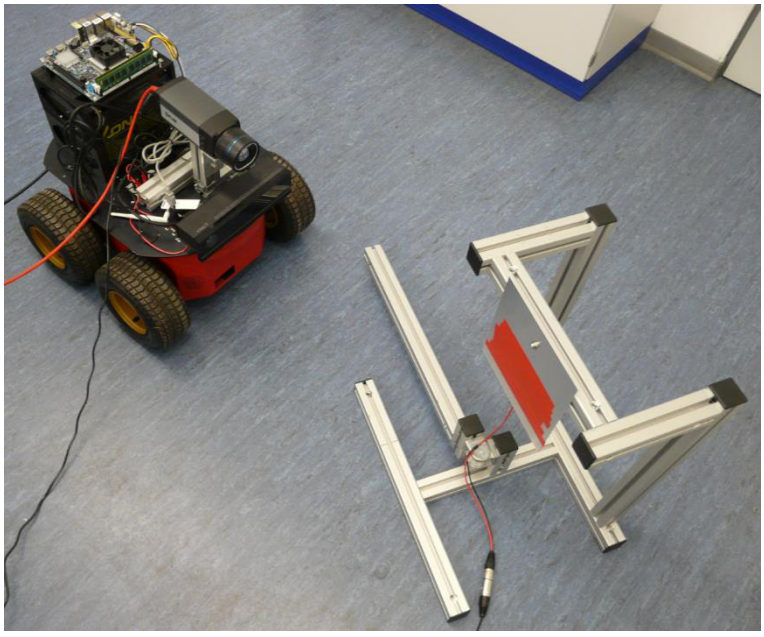

Figure 11: Experimental setup during mobile robot evaluation. The Pioneer 2 equipped with the FLIR A655sc thermal imaging camera a Kinect v2 depth sensor looking at the heated aluminum plate.

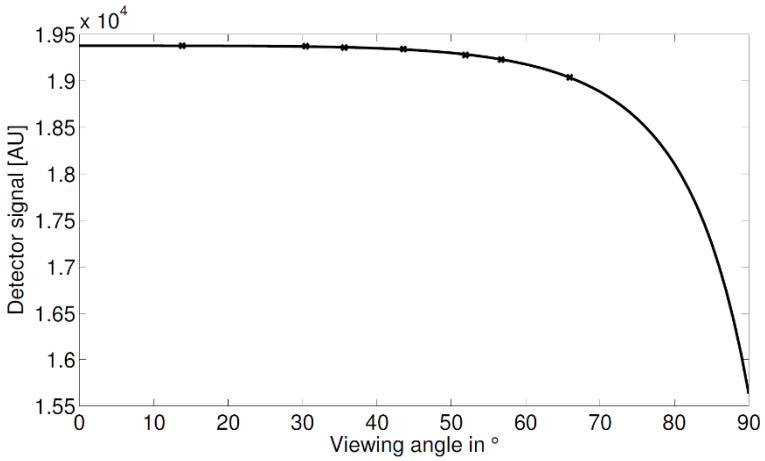

Figure 12: Dielectric surface point in the mobile robot evaluation: detector signal graph based on estimated parameters n, T_{obj} and T_{amb} (solid line); points (x) mark the measured values.

$Err(T_{amb}) = 7.22\ K$ with regard to the thermometer values. We refer these errors primarily to inaccuracies in the determination of the viewing angle.

4. Handling Thermal Reflections

As mentioned in Section 2.2, there are various approaches in order to detect and remove reflections from thermal images. In the following, due to the limitations that come along with our application, only software-based methods are considered. The other discussed possibilities are not applicable because of multiple reasons. For an autonomous acting robot, it is unpractical to cover regarded surfaces with high-emissivity materials in order to avoid reflections. Additionally, for the use of infrared polarizing filters a strict spatial setup of the camera, filter and surface is needed. While this is useful under laboratory conditions and for manual thermography, the approach does not meet the demands of flexibility in real world scenarios.

In this section, we first give an overview on known software-based methods to detect and remove reflections. These approaches are designed to work for RGB images and it is difficult to transfer them to thermal images. Therefore, we then present a method for thermal reflection detection and removal.

4.1 Overview on Software-based Approaches

The general procedure of software-based approaches to reflection handling is to separate different layers of the input image. What distinguishes the work of different authors is the method they use to separate these layers. Before we present our approach, we give a little review on the various methods of layer separation and specular highlight removal. Following, we also explain why most of the approaches are not applicable to the SmokeBot project.

One way of layer separation is to manually mark key points in the reflection/background layer as presented in [11]. This user-assisted, single-image approach comes along with the disadvantage that every individual image has to be edited manually. Besides the fact that this would take a long time, the method is not viable due to autonomy reasons.

Another method of layer separation uses independent components analysis [13]. Taking two images of the same scene but with different polarizer settings, the approach is able to separate the components of the images. Similar approaches taking input images of the same scene make use of changing focus settings [21] or apply a flash [22]. However, these methods are not applicable to SmokeBot, because of the moving robot that shall not stop its movement in order to take images.

There are also possibilities to exploit the robot movement and the resulting change of the camera's point of view. Comparing the movement of different image features allows extracting layers, because features tracked in distinct spatial depths move differently. In the context of using image sequences to separate background and reflection layers, approaches have been presented in [23], [14] and [24]. For thermal images, a challenge lies in detecting and tracking of features. This makes it hard to transfer the presented implementations from RGB to thermal images.

In [25] and [26], methods for removing specular highlights in RGB images have been proposed. The authors use illumination chromaticity in order to separate diffuse and specular image layers.

Due to the lack of color information in thermal images, these methods are not applicable to the SmokeBot project.

4.2 Detection and Removal of Thermal Reflections

Similar to some of the previously discussed works, we make use of the camera's changing point of view. In contrast to the presented approaches, we assume that the 3D model of the regarded surface structure is known. In later stages of the SmokeBot project, this environment model will be provided by Simultaneous Localization and Mapping (SLAM) algorithms. In the project's current stage, we simplified the environment model by regarding only a plane reflective plate that is recognized by its corner points. This way, we were able to relate the measured intensity values to spatial points.

The proposed implementation includes the following steps:

1) Detection of the corners of the reflective plate. This step is redundant in case of an environment model being provided.
2) Thermal image rectification allows creating a grid of intensity/temperature cells.
3) Reflection detection using differences of consecutive images.
4) Image back-transformation highlighting/removing thermal reflections.

The most significant steps are described in the following sections.

4.2.1 Temperature Grid Generation

In this step, we assume that the geometrical relation between the 3D surface structure and the thermal image is known, i.e. that the thermal image is already mapped on the surface. Since we only consider a plane reflective plate in this implementation, we first dewarp the plate. After that, the plate surface is downsampled to a user-defined grid.

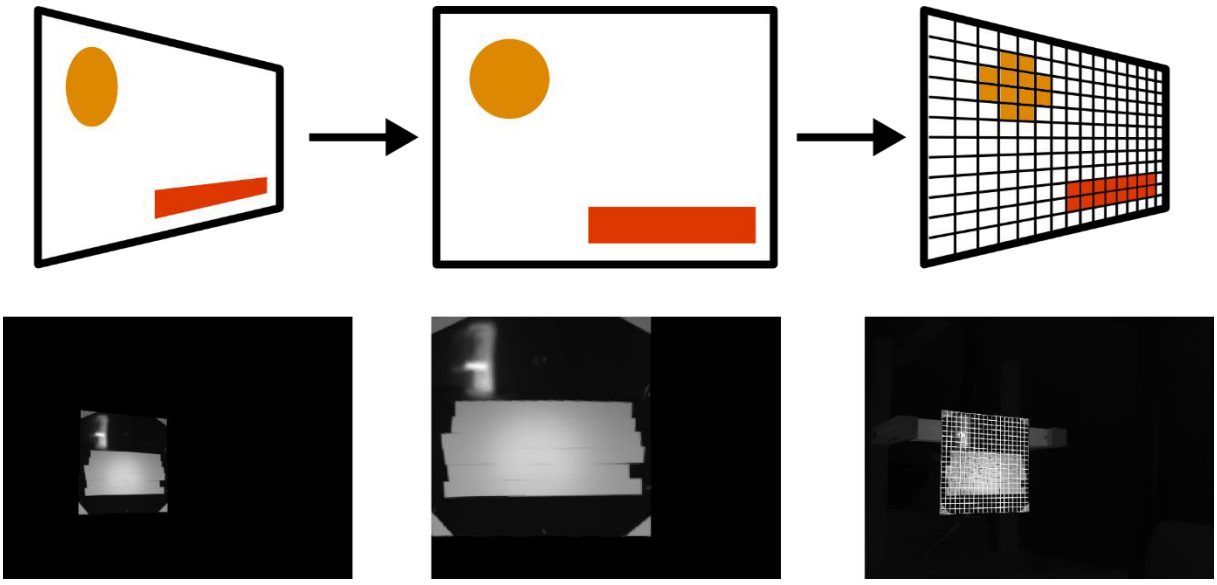

Figure 13: Temperature grid generation: Sketches on top of the figure show the functional principle of the grid generation. On the bottom, corresponding examples are depicted. See text for a more detailed explanation.

Figure 13 depicts the working principle of the implementation with the aid of an example. The geometrically distorted image is dewarped (i.e. rectified) in the first step. Notice, that only the region of interest (the heated aluminum plate) is rectified in the second example image. After that, a grid whose size can be defined by the operator is generated and laid on top of the image. Depending on the grid size, the spatial resolution of the resulting image is different from the resolution of the input image.

4.2.2 Reflection Detection

The implemented approach on reflection detection is based on background subtraction. Calculating a moving average over the image sequence leads to a background image that can be subtracted from the current thermal image. After some postprocessing (thresholding, opening, etc.), the reflection can be marked in the final image.

In Figure 14, the working principle of the background subtraction is depicted. In order to calculate the moving average of the scene, images from previous iterations are summed up in a weighted addition. The current image has less weight than the current moving average image in our implementation. That means that the current image has less influence on the result than the sum of all previous images. This leads to an image (see the center bottom image of Figure 14), in which static objects are more clear and sharp than moving objects (which are blurred and less intense).

A special feature of our implementation is the reflection feedback. The reflection image I_{refl} is used as a mask for the accumulation (weighted addition) algorithm. This way, we prevent reflections detected in the current image from being included in the moving average calculation. In the current stage of the implementation, only moving reflections can be detected directly (i.e.

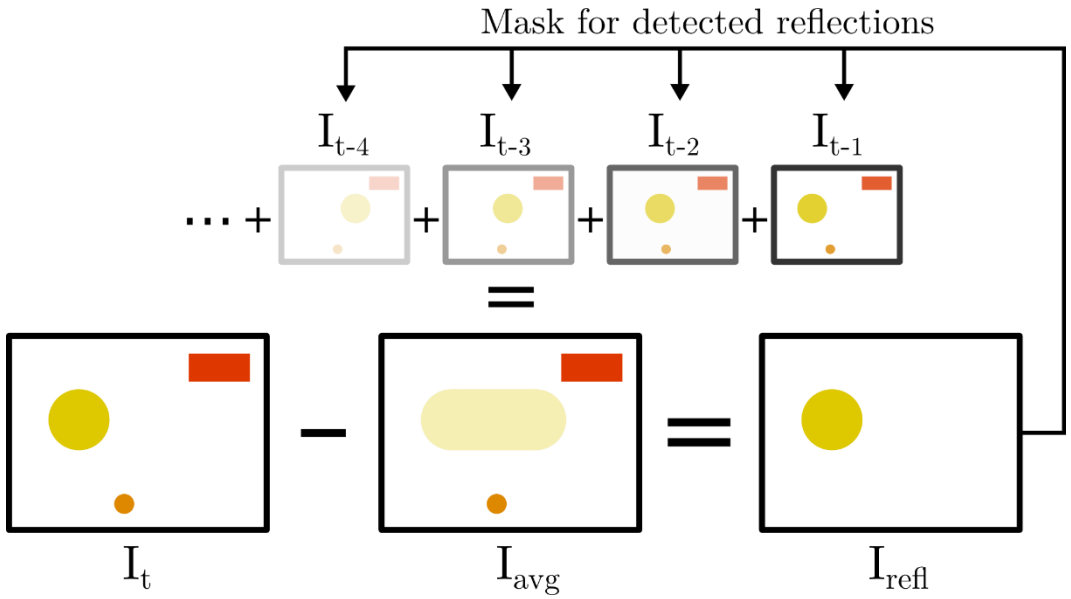

Figure 14: Functional principle of reflection detection used in our implementation. Moving average image I_{avg} is subtracted of the current image I_t to obtain the reflection I_{refl}. The reflection image is fed back into the accumulation algorithm that calculates the moving average image.

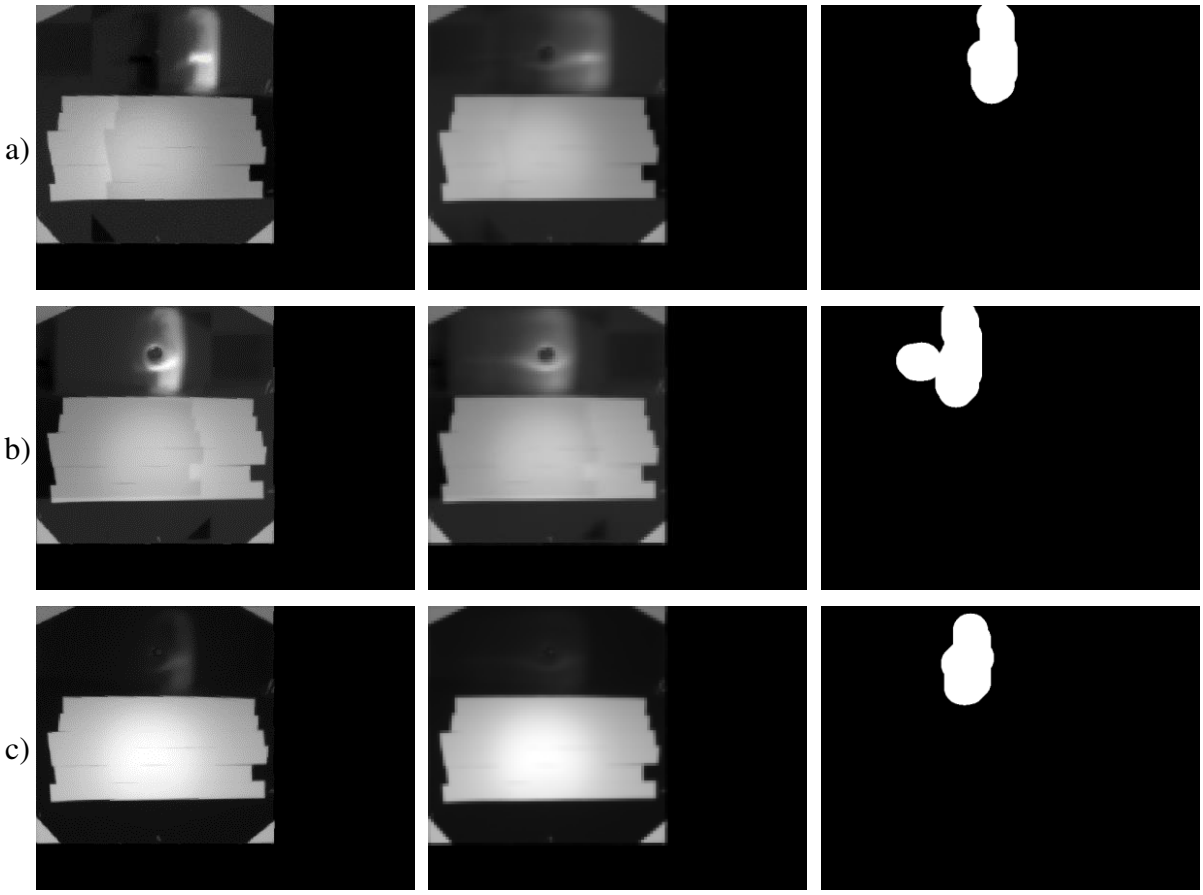

Figure 15: Examples on reflection detection: The three rows show three different datasets. In the left column, the raw thermal image can be seen. The middle column shows the moving average image. The right column depicts the calculated thermal reflection.

the thermal imaging camera must be moving). For later stages of the project, it is conceivable to track reflections removing them in the resulting image.

To evaluate our approach, we took three exemplary datasets. All images show a heated aluminum plate with duct tape on it. The high-emissivity duct tape serves as a static object related to the plate, which means that it (optimally) does not move in consecutive, rectified images of the plate. This is different for the remaining low-emissivity surface area of the plate. Here, it is possible to see reflections such as the heated can that we used in our experiments. The results of the reflection detection for the different datasets are shown in Figure 15.

4.2.3 Reflection Removal

Reflection removal is done with the help of the reflection image that was output by the reflection detection algorithm. For the pixels marked as reflections (i.e. the white areas in the reflection image), the corresponding pixel in the final image is filled with the pixel's moving average instead of the current pixel value. If the pixel in the reflection image is not marked as a reflection, the final image pixel value is chosen according to the latest thermal image.

Figure 16 shows exemplary images taken from the three datasets. It can be seen that – especially in the third example – the reflection can be removed almost completely. The first and the second example show small contours of the reflection that are not removed correctly. Most likely, this

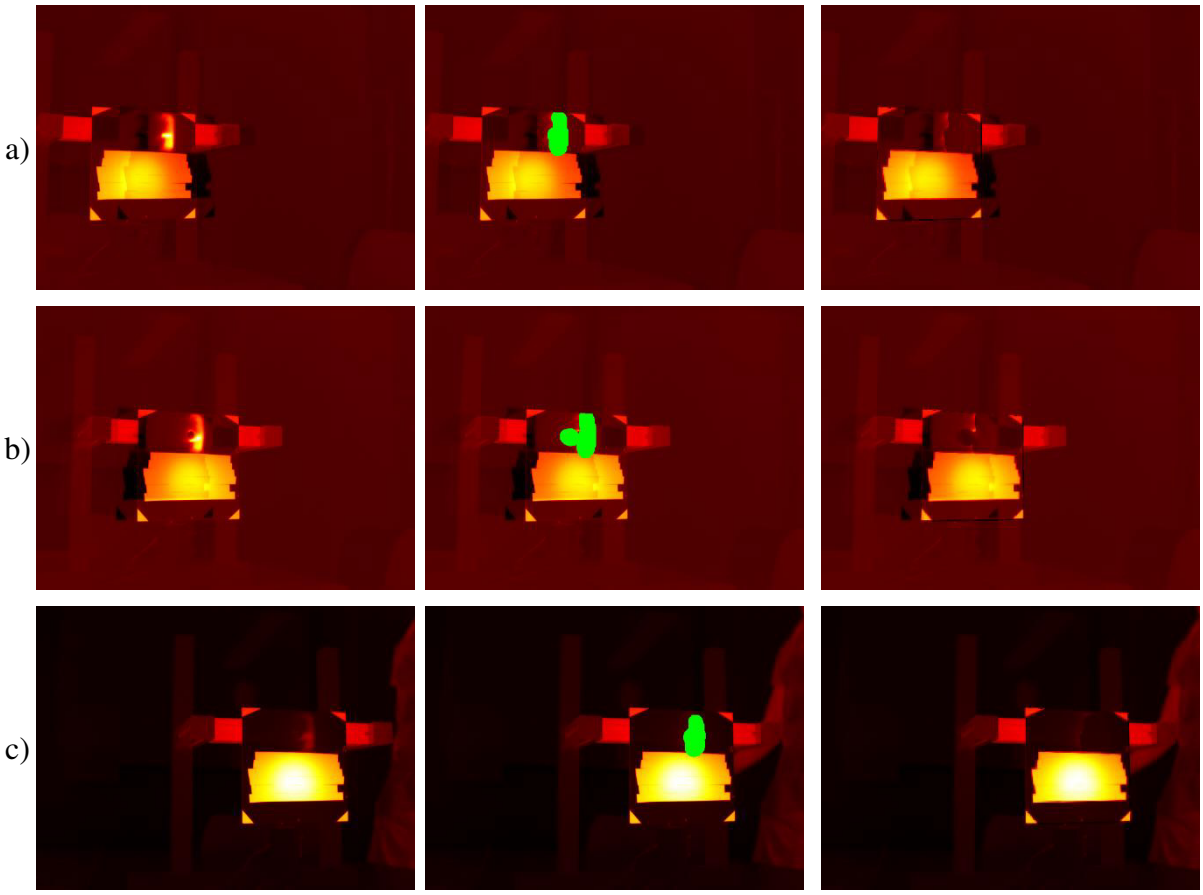

Figure 16: Examples on reflection removal: The three rows show three different datasets. In the left column, the raw thermal image can be seen. The middle column shows the thermal image with highlighted reflections. The right column depicts the thermal image with reflections removed.

can be avoided tweaking the parameters such as the mask size of the dilation operation that inflates the detected reflection in the reflection image.

5. Influence of Smoke

We evaluated the influence of smoke on thermal images using a smoke machine, or more precisely a fog machine[1]. We decided to perform our experiments this way due to several reasons:

- Fog machines are broadly used in firefighting training; also in "hot" training situations, where the fog is heated with the help of a gas burner or something similar.
- The smoke output can be controlled, which makes the experiments more deterministic and reproducible.
- The smoke is toxicologically harmless to humans.

As stated before, it was already shown in other works that dense, low-temperature smoke as well as light, high-temperature smoke do not significantly influence thermal images. This observation can be explained using Equation (4) that was introduced in the thermography basics of this report. Neglecting the emissivity's influence (i.e. assuming $\varepsilon = 1$), the radiation measured by the thermal imaging camera can be calculated as:

$$I_{sum} = \tau I_{obj}^{bb} + (1-\tau) I_{atm}^{bb} = \tau\left(I_{obj}^{bb} - I_{atm}^{bb}\right) + I_{atm}^{bb}. \quad (9)$$

Equation (9) shows that both high temperature and transmittance are closely related. For dense, low-temperature smoke (related to the target temperature) the assumptions $I_{atm}^{bb} \ll I_{obj}^{bb}$ respectively $\tau < 1$ hold and the equation simplifies to $I_{sum} = \tau I_{obj}^{bb}$. This means that for dense, low-temperature smoke conditions, the measured signal is at most slightly attenuated depending on transmittance τ. Similar considerations can be performed assuming light ($\tau \approx 1$), high-temperature smoke. In this case, the equation simplifies to $I_{sum} = I_{obj}^{bb}$.

In the experiments presented in this section, we first verify the considerations about dense, low-temperature smoke. After that, we evaluate the influence of dense and hot smoke.

5.1 Dense, Low-Temperature Smoke

This experiment was performed using a smoke machine in combination with high-density smoke fluid. The smoke was carried into a cardboard frame that acted as a windbreak. The thermal imaging camera observed a heated target that was placed inside/behind the frame. Figure 17 and Figure 18 show the experimental setup. As can be seen from the pictures, it is not possible to see through the smoke with a standard RGB camera. However, in the thermal image, the target can be seen clearly (see Figure 19).

[1] In the following, we use the words „fog" and „smoke" synonymously, although we are aware of the different meanings in the sense of physics.

Figure 17: Low-temperature smoke experiment: Smoke is carried into a cardboard frame that serves as a windbreak. Inside the frame, there is a heated target.

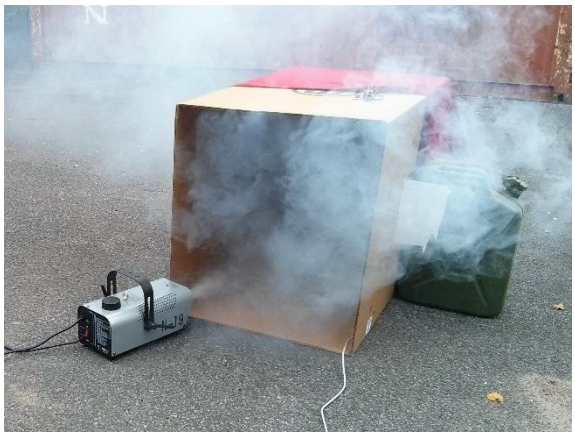

Figure 18: Same scene as in Figure 17, but with smoke applied.

The evaluation was performed measuring the target temperature over time. No significant changes could be measured. This confirms the considerations discussed previously. Measuring the changes in temperature directly in front of the smoke machine's nozzle resulted in slightly higher temperatures when smoke was applied compared to a no-smoke situation. This temperature change is caused by the fact that the smoke is still warm/hot when leaving the smoke machine. Inside the smoke machine the smoke fluid is vaporized at temperatures above $200\,°C$.

5.2 Dense, High-Temperature Smoke

For this evaluation, we used a slightly different experimental setup. The smoke was not directly blown into the target area, but carried through a metal pipe. The pipe was heated by a gas burner placed below. With this setup, it was possible to heat up the smoke to about $330\,K$ ($57\,°C$). The experimental setup is depicted in Figure 20 and Figure 21.

Figure 19: Low-temperature smoke experiment: Exemplary thermal image.

Figure 20: High-temperature smoke experiment: Smoke is carried through a pipe and heated by a gas burner. A cardboard frame serves as a windbreak. Inside the frame, there is a heated target.

Figure 21: Same scene as in Figure 20, but with smoke applied.

Altogether, we took four datasets. In the first two datasets, we demonstrated the influence of hot smoke (compared to the target temperature) on a human behind it. The purpose of these two datasets is simple visual evaluation. In Figure 22, a series of image pairs (RGB and thermal) is depicted. Especially subfigures b) and c) show that there can be misinterpretations in the thermal images caused by smoke. The heated smoke seems to cover the human that crouches in the background. For better visibility (especially contrast), we chose the “rainbow” color map to artificially colorize the images.

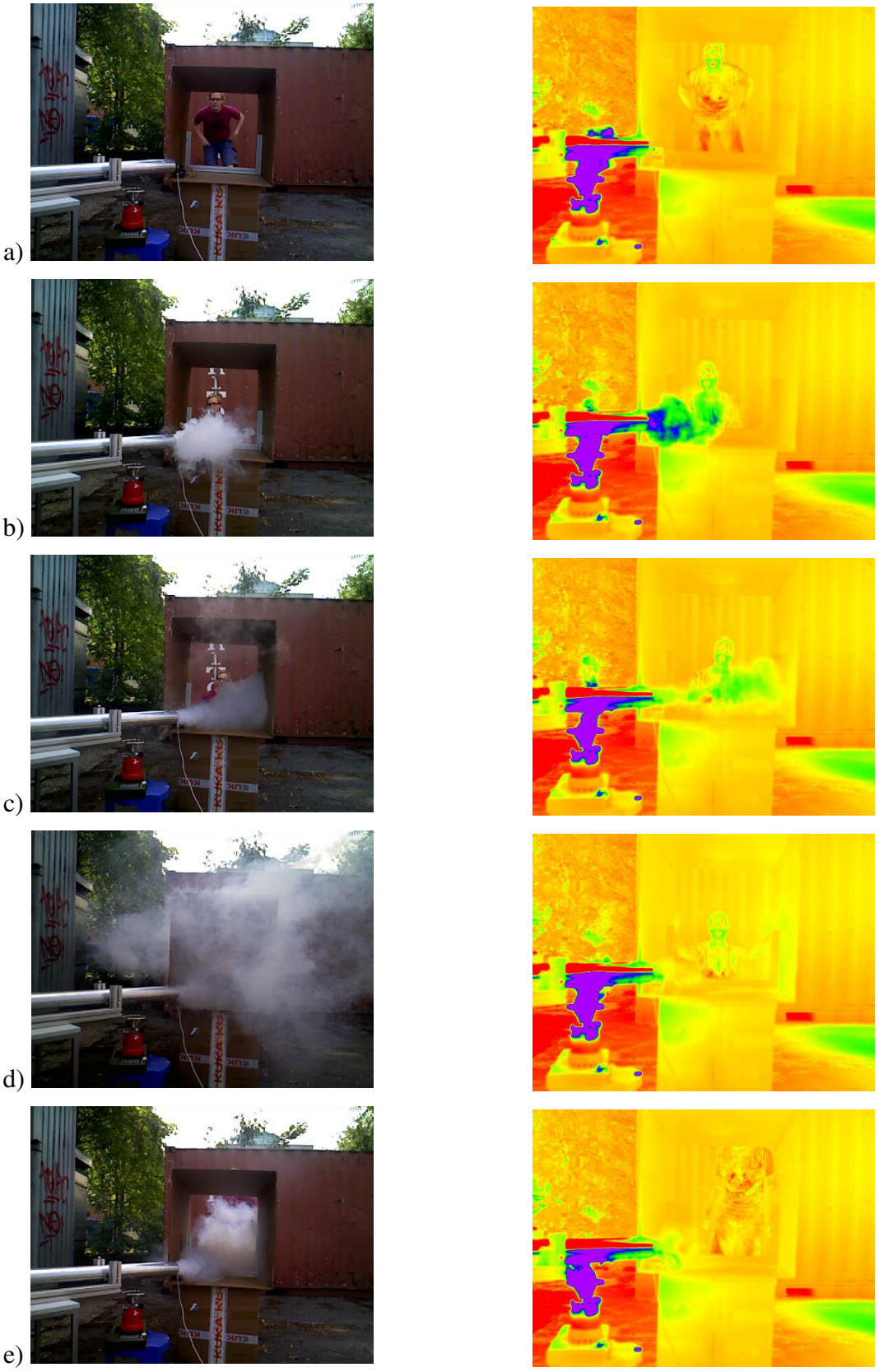

Figure 22: High-temperature smoke experiment: Comparison between RGB image (left) and thermal image (right) for several points in time (dataset 1).

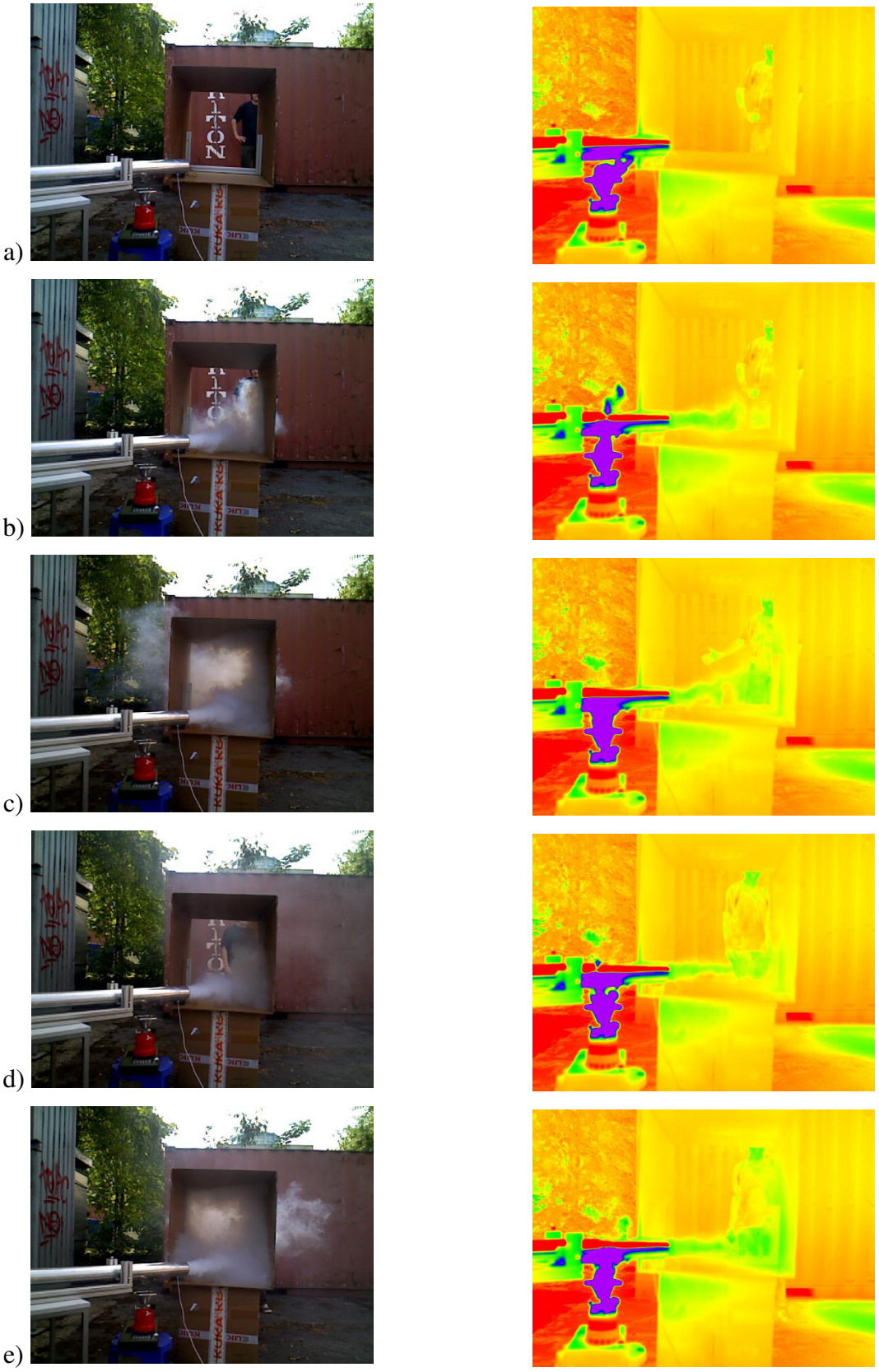

Figure 23: High-temperature smoke experiment: Comparison between RGB image (left) and thermal image (right) for several points in time (dataset 2).

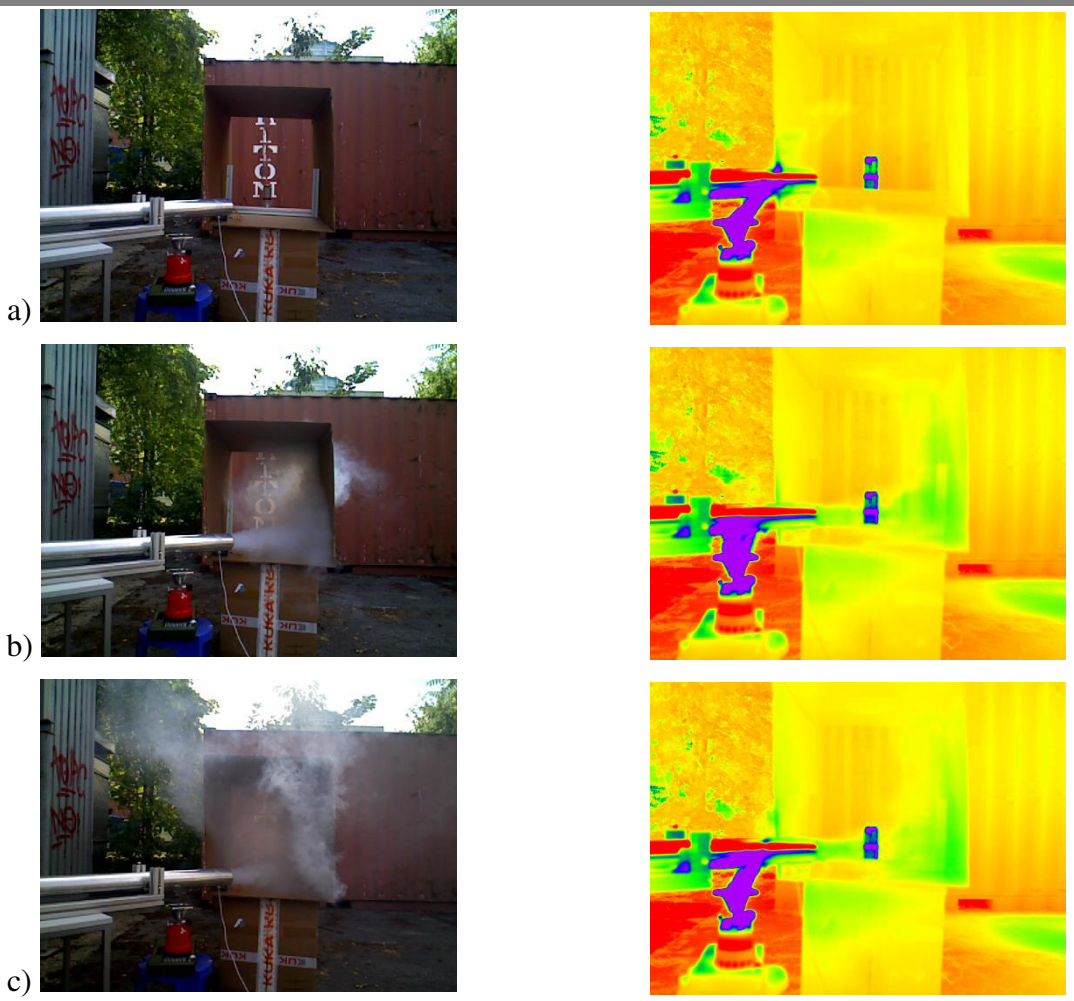

Figure 24: High-temperature smoke experiment: Comparison between RGB image (left) and thermal image (right) for several points in time (dataset 3).

Similar result are shown in Figure 23. Especially on subfigures b) to e) the heated smoke is visible. A distinction between the smoke and the person's legs/pants is barely possible.

In the other two datasets, we evaluated the smoke's influence more objectively. Considering a static target (heated up to about 346 K), we observed the target temperature change over

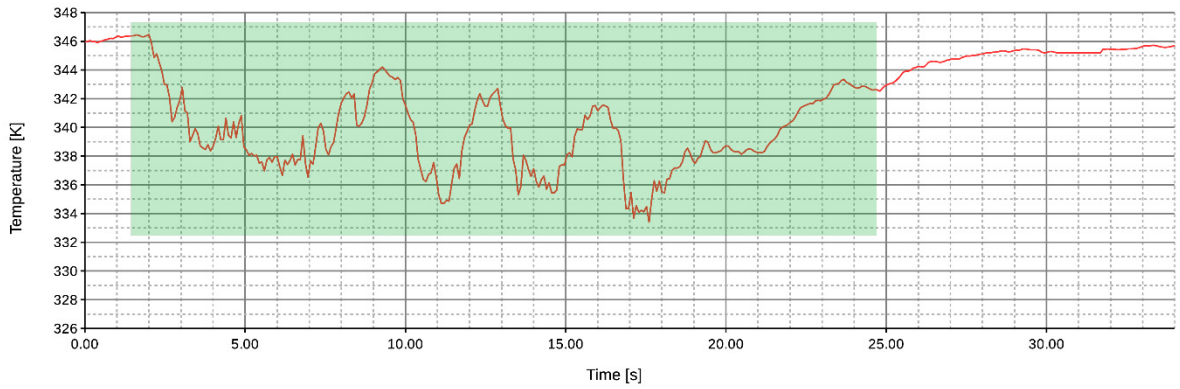

Figure 25: Temperature graph for dataset 3 during high-temperature smoke experiment. Green areas represent durations in which smoke influenced the measurement.

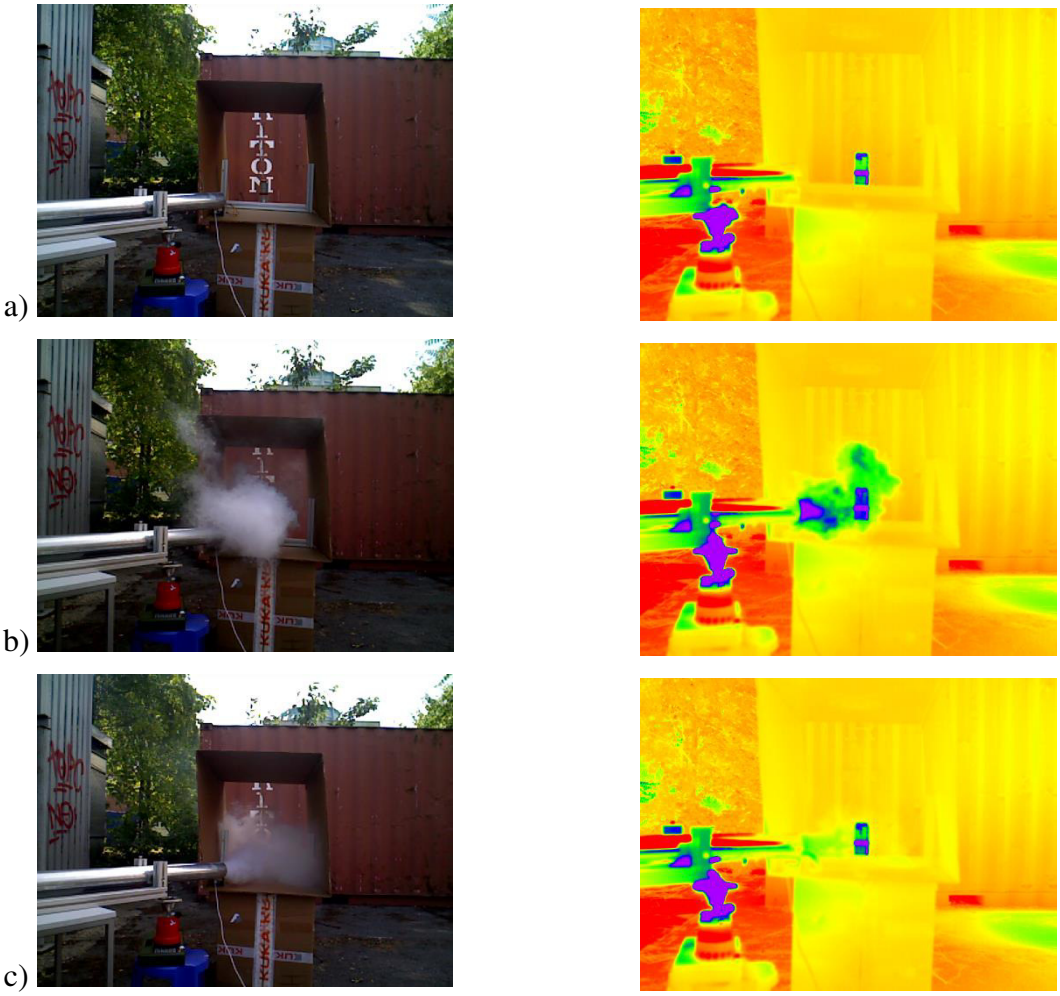

Figure 26: High-temperature smoke experiment: Comparison between RGB image (left) and thermal image (right) for several points in time (dataset 4).

time when applying smoke. Some of the images taken are depicted in Figure 24. The temperature graph of dataset 3 is shown in Figure 25. It can be seen that the temperature measured without any smoke influence is at about 346 K. The green area in the graph represents

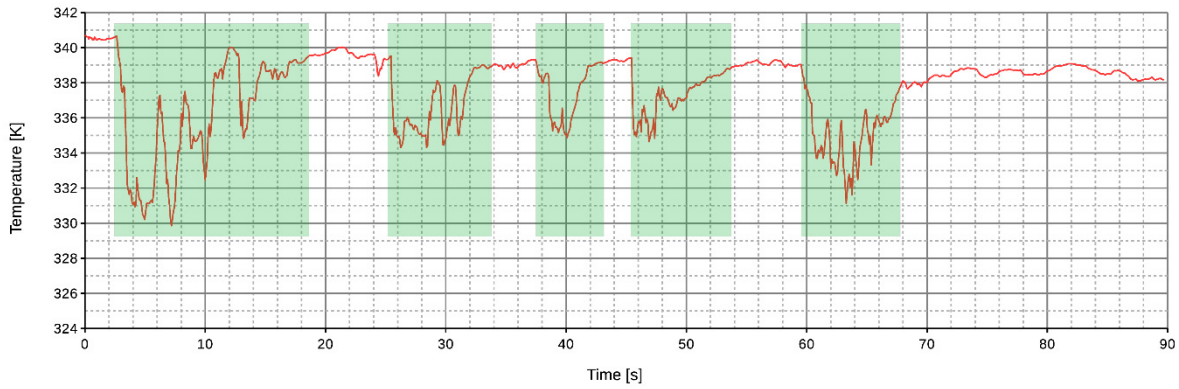

Figure 27: Temperature graph for dataset 4 during high-temperature smoke experiment. Green areas represent durations in which smoke influenced the measurement.

the duration in which the smoke machine applied smoke to the scene. During this period of time, the measured temperature strongly varies and drops below $336\ K$ temporarily.

This behavior can be seen more clearly in dataset 4. There, we applied the smoke interval-wise. Figure 26 partially shows the series of images taken for dataset 4. The corresponding temperature graph is depicted in Figure 27. As can be seen from the graph, the smoke influences the measurement when it is applied. The temperature decreases to a minimum of $330\ K$. In the periods where no smoke is applied, the measured temperature stabilizes at about $339\ K$. This stabilization also happens when there is still smoke visible in the RGB image. We refer this behavior to the fact that the smoke cools down to ambient temperature very fast. Only in the moments when it leaves the smoke machine respectively the pipe, its temperature is high enough to influence the measurement.

6. Conclusion and Future Work

In this technical report, we investigated typical misinterpretations of images taken by a thermal imaging camera. Explaining the basic principles of thermography, we gave a state-of-the-art overview on three different sources of error:

- Unknown emissivity values,
- Thermal reflections and
- Smoke in the line of sight between the camera and the regarded surface.

Regarding unknown emissivity values, it was shown that a varying viewing angle of the camera can be exploited in order to correct misinterpretations of low-emissivity surface areas. Considering the intensities depending on the viewing angle, we were able to do a basic material classification and to estimate emissivity and temperature values.

The detection and removal of thermal reflections was implemented using a background subtraction approach. Calculating the moving average over all past images and subtracting it from the current thermal image, we were able to detect reflection areas in the scene. We showed that – in combination with a reflection feedback provided to the accumulation function – our algorithm is able to eliminate moving reflections in thermal images.

Both the approaches in handling misinterpretations due to unknown emissivities and thermal reflections rely on the availability of a 3D model of the environment. The temperature values provided by the thermal imaging camera must be mapped onto this 3D structure. Since at the current stage of the SmokeBot project no such environment model was available, we used a strict experimental setup and known geometrical relations to compensate for this.

The third source of misinterpretations investigated in our experiments is the influence of dense smoke on thermal images. In the first evaluation, we could confirm that dense, low-temperature smoke has no significant influence on thermal images. The second experiment showed that dense, high-temperature smoke in contrast does influence the measurements.

During the next year, we will develop a software toolkit that allows indoor surface temperature mapping (Task 3.2). With the help of this, we will be able to transfer our approaches to the real use case scenario. Regarding the correction of low-emissivity temperature measurements, it could be investigated how to preferably deal with present reflections at the same time. Our approach to reflection removal could furthermore be extended by a reflection tracking mechanism, that additionally allows to eliminate static reflections that were already detected. In later stages of the project, misinterpretations caused by dense, hot smoke may be eliminated with the help of other sensors. It is conceivable, that the comparison of different sensor data can lead to information about highly probable smoke areas, which can then be marked and removed in the current thermal images.

References

[1] H. Mano, K. Kon, N. Sato, M. Ito, H. Mizumoto, K. Goto, R. Chatterjee, and F. Matsuno, "Treaded control system for rescue robots in indoor environment," 2009, pp. 1836–1843.

[2] M. Zaheer Aziz and B. Mertsching, "Survivor search with autonomous UGVs using multimodal overt attention," 2010, pp. 1–6.

[3] L. Merino, F. Caballero, J. R. Martínez-de Dios, J. Ferruz, and A. Ollero, "A cooperative perception system for multiple UAVs: Application to automatic detection of forest fires," *J. Field Robot.*, vol. 23, no. 3–4, pp. 165–184, Mar. 2006.

[4] D. W. Casbeer, R. W. Beard, T. W. McLain, S.-M. Li, and R. K. Mehra, "Forest fire monitoring with multiple small UAVs," in *American Control Conference, 2005. Proceedings of the 2005*, 2005, pp. 3530–3535.

[5] F. Amon, A. Hamins, and J. Rowe, "First responder thermal imaging cameras: establishment of representative performance testing conditions," 2006, p. 62050Y–62050Y–12.

[6] A. Ianiro and G. Cardone, "Measurement of surface temperature and emissivity with stereo dual-wavelength IR thermography," *J. Mod. Opt.*, vol. 57, no. 18, pp. 1708–1715, Oct. 2010.

[7] J. R. Howell, R. Siegel, and M. P. Mengüç, *Thermal radiation heat transfer*, 5th ed. Boca Raton: CRC Press, 2011.

[8] J. Thevenet, M. Siroux, and B. Desmet, "Measurements of brake disc surface temperature and emissivity by two-color pyrometry," *Appl. Therm. Eng.*, vol. 30, no. 6–7, pp. 753–759, May 2010.

[9] Z. Li, W. Yao, S. Lee, C. Lee, and Z. Yang, "Application of infrared thermography technique in building finish evaluation," *J. Nondestruct. Eval.*, vol. 19, no. 1, pp. 11–19, 2000.

[10] M. Vollmer, S. Henke, D. Karstädt, K. P. Möllmann, and F. Pinno, "Identification and suppression of thermal reflections in infrared thermal imaging," *InfraMation Proc.*, 2004.

[11] A. Levin and Y. Weiss, "User Assisted Separation of Reflections from a Single Image Using a Sparsity Prior," *IEEE Trans. Pattern Anal. Mach. Intell.*, vol. 29, no. 9, pp. 1647–1654, Sep. 2007.

[12] H.-L. Shen, H.-G. Zhang, S.-J. Shao, and J. H. Xin, "Chromaticity-based separation of reflection components in a single image," *Pattern Recognit.*, vol. 41, no. 8, pp. 2461–2469, Aug. 2008.

[13] H. Farid and E. H. Adelson, “Separating reflections and lighting using independent components analysis,” in *Computer Vision and Pattern Recognition, 1999. IEEE Computer Society Conference on.*, 1999, vol. 1.

[14] R. Szeliski, S. Avidan, and P. Anandan, “Layer extraction from multiple images containing reflections and transparency,” in *Computer Vision and Pattern Recognition, 2000. Proceedings. IEEE Conference on*, 2000, vol. 1, pp. 246–253.

[15] Kun Gai, Zhenwei Shi, and Changshui Zhang, “Blind Separation of Superimposed Moving Images Using Image Statistics,” *IEEE Trans. Pattern Anal. Mach. Intell.*, vol. 34, no. 1, pp. 19–32, Jan. 2012.

[16] J. W. Starr and B. Y. Lattimer, “Evaluation of Navigation Sensors in Fire Smoke Environments,” *Fire Technol.*, vol. 50, no. 6, pp. 1459–1481, Nov. 2014.

[17] J. F. Widmann and J. Duchez, “The effect of water sprays on fire fighter thermal imagers,” *Fire Saf. J.*, vol. 39, no. 3, pp. 217–238, Apr. 2004.

[18] J.-H. Kim and B. Y. Lattimer, “Real-time probabilistic classification of fire and smoke using thermal imagery for intelligent firefighting robot,” *Fire Saf. J.*, vol. 72, pp. 40–49, Feb. 2015.

[19] M. Martiny, R. Schiele, M. Gritsch, A. Schulz, and S. Wittig, “In situ calibration for quantitative infrared thermography,” in *QIRT*, 1996, vol. 96, pp. 3–8.

[20] J. C. Lagarias, J. A. Reeds, M. H. Wright, and P. E. Wright, “Convergence Properties of the Nelder--Mead Simplex Method in Low Dimensions,” *SIAM J. Optim.*, vol. 9, no. 1, pp. 112–147, Jan. 1998.

[21] Y. Y. Schechner, N. Kiryati, and R. Basri, “Separation of transparent layers using focus,” *Int. J. Comput. Vis.*, vol. 39, no. 1, pp. 25–39, 2000.

[22] A. Agrawal, R. Raskar, S. K. Nayar, and Y. Li, “Removing photography artifacts using gradient projection and flash-exposure sampling,” in *ACM Transactions on Graphics (TOG)*, 2005, vol. 24, pp. 828–835.

[23] A. Criminisi, S. B. Kang, R. Swaminathan, R. Szeliski, and P. Anandan, “Extracting layers and analyzing their specular properties using epipolar-plane-image analysis,” *Comput. Vis. Image Underst.*, vol. 97, no. 1, pp. 51–85, Jan. 2005.

[24] Y. Li and M. S. Brown, “Exploiting Reflection Change for Automatic Reflection Removal,” 2013, pp. 2432–2439.

[25] R. T. Tan and K. Ikeuchi, “Separating reflection components of textured surfaces using a single image,” *Pattern Anal. Mach. Intell. IEEE Trans. On*, vol. 27, no. 2, pp. 178–193, 2005.

[26] C. Jung, L. Jiao, and H. Qi, “Specular highlight removal using reflection component separation and joint bilateral filtering,” in *Intelligent Science and Intelligent Data Engineering*, Springer, 2012, pp. 513–521.

Improving the Interpretation of Thermal Images with the aid of Emissivity's Angular Dependency

Björn Zeise, Sebastian P. Kleinschmidt and Bernardo Wagner
Institute of Systems Engineering - Real Time Systems Group
Leibniz Universität Hannover, Appelstr. 9A, D-30167 Hannover, Germany
zeise | kleinschmidt | wagner @rts.uni-hannover.de

***Abstract*— Autonomous mobile robots exploring areas in a search and rescue (SAR) context benefit greatly from the usage of thermal imaging cameras (TICs). In unknown environments, the interpretation of the temperature values provided by the camera is a challenge. This is due to the fact that temperature calculation based on thermal images depends strongly on the regarded surface emissivity. In this work, we show how to improve the temperature interpretation in thermal images making use of the diverse characteristics of the emissivity at varying viewing angles. Using several thermal images taken from different points of view, we are able to do a basic material classification. In combination with an algorithm that maps temperature values on the environment's 3D structure, we estimate the regarded surface emissivity and temperature. The presented approach is evaluated by a single camera setup using nonlinear optimization techniques.**

I. Introduction

Recent disasters such as the September 11 attacks or the Fukushima Daiichi nuclear disaster have shown that mobile robots can be used to efficiently support human rescue forces (see [1], [2]). Search and rescue (SAR) robots can visit areas, that cannot be explored by humans due to several reasons – in some situations it is too dangerous to go there (potential collapse, contamination, etc.), in other cases the rescue forces simply cannot reach the target zone because of their body size. In [3], we presented an interdisciplinary approach to autonomous team-based multi-robot exploration in such scenarios.

SAR robots are typically equipped with several sensors that proved beneficial in these kinds of scenarios (RGB cameras, laser scanner, gas sensors, etc.). Over the past years, thermal imaging cameras (TICs) have become important components in robotic systems – mostly in the field of SAR robotics. In this context, TICs are particularly used to detect victims at disaster sites (e.g. [4], [5]), but also to explore forest fires (e.g. [6], [7]). Either the robots operate remotely controlled by human operators or they act fully autonomously.

While nowadays SAR robots mostly operate under remote control, there are good reasons for the robots to have autonomous features, not only in motion planning and control but also in the field of environment perception. In a typical remote control scenario the operator himself is able to evaluate the information he gets from the robot sensors. For autonomous robots this is different, because, in difficult situations, they cannot rely on reasoning methods (like a human operator). Therefore, the robots need reliable mechanisms to model their environment and store the important information (e.g. [8]).

Basically, a human operator would certainly be able to recognize ambiguities caused by highly reflective surfaces and resulting mirror effects or misinterpretations of temperatures due to unknown emissivities. For an autonomously acting robot however, the correct interpretation of temperature information is a massive problem.

Our goal is to reduce misinterpretations of temperature values measured by a mobile robot equipped with a TIC. The improvement shall be achieved regarding temperature misinterpretations due to unknown surface emissivity values in unexplored environments. A typical use case for the approach presented in this work is the operation of an autonomously acting SAR robot exploring a laboratory in which a fire has broken out. Somewhere in this laboratory there are hot gas bottles, whose temperatures are not correctly interpreted due to their metal surface. For this reason, the robot is not able to recognize the potential hazard. Our approach will significantly improve the robot's ability to correctly identify the situation.

The remainder of this paper is organized as follows: In Section II, we give an overview on related thermography research topics, especially on emissivity/temperature estimation and temperature mapping. Section III explains the thermography basics on which the presented work is founded. In Section IV, our approach is described, followed by an evaluation (Section V) and conclusion (Section VI).

II. Related Work

The need to estimate surface emissivities arises especially when no additional contactual temperature measurement can be taken or when the regarded surface cannot be investigated under laboratory conditions. This is e.g. the case in temperature measurements of land/sea surfaces taken by satellites (e.g. [9], [10]), flames (e.g. [11], [12]) and hot metals in industrial processes (e.g. [13], [14]).

A common method to estimate surface emissivity and real temperature is based on the use of two measurement systems working in different wavelength bands. This is also referred to as the *two-color* or *ratio method*. In [15], this method is used to create a surface mesh of a heated sphere, whose

Accepted at 2015 IEEE International Symposium on Safety, Security, and Rescue Robotics (SSRR)

nodes' emissivities and temperatures can be calculated using least square minimization. For this purpose, optical constants are estimated in order to calculate an emissivity graph.

The effect of a varying viewing angle while taking measurements with a TIC has been investigated e.g. by [16] and [17]. While the authors of these papers only consider materials with dielectric emissivity characteristic, [18] also evaluates the viewing angle dependency of metal emissivities. We, too, consider both metal and dielectric materials.

Mapping of thermal images on 3D structures has been a recent research topic and was investigated by multiple authors. [19] presents a handheld system combining a TIC and a RGB-D sensor. Using a multi-variable weighted raycasting algorithm that implicitly removes the effect of unknown emissivities allows the authors to create 3D models with temperature surface maps. [20] shows another approach to temperature mapping, where a tilted 2D laser scanner is used together with a TIC in order to help rescue forces to locate victims. In our mapping approach, we use the combination of a TIC and a RGB-D sensor.

III. Thermography Basics

In thermodynamics, there are three different types of heat transfer: conduction, convection and radiation. The underlying principle of thermography is radiation heat transfer. Each body whose temperature is above absolute zero ($0\ K$) emits radiation. According to the third law of thermodynamics, this statement applies to each real body. An idealized model of a body that absorbs all incident radiation energy simultaneously emitting it again is called *black body*.

The spectral intensity I^{bb} emitted by a black body can be calculated using Planck's law:

$$I^{bb}(\lambda, T) = \frac{2\pi hc^2}{\lambda^5 \left(\exp\left(\frac{hc}{\lambda kT}\right) - 1\right)}. \tag{1}$$

The constants characterizing Equation 1 are Planck's constant h and Boltzmann constant k. Additionally, the speed of light c is also assumed to be constant. Hence, the spectral black body intensity depends only on the body's temperature T and the radiation's wavelength λ.

As written above, a black body is an idealized physical model. Real bodies do not absorb all incident radiation. Instead, they might reflect a part of the incoming radiation or transmit it through the body. In our work, the transmission of radiation is neglected, because we only consider opaque bodies. The ratio between the emitted spectral intensity I^{real} of a real body and the emitted spectral intensity I^{bb} of a black body at the same temperature is called *emissivity* ε:

$$\varepsilon(\lambda, T, \Theta) = \frac{I^{real}(\lambda, T, \Theta)}{I^{bb}(\lambda, T)}. \tag{2}$$

Surface emissivity mainly depends on the regarded wavelength λ, the surface temperature T and the viewing angle Θ. In this work, we will not consider wavelength dependencies, because in our experiments we assume the regarded surfaces to be *gray*, which means that their emissivity does not depend on wavelength (see [21, p. 65]). All subsequent statements in the presented work are based on measurements taken in the spectral range between $7.5\ \mu m$ and $14\ \mu m$. Also the diverse emissivity behavior regarding different surface temperatures (see [21, pp. 110 - 120]) is neglected for simplicity purposes.

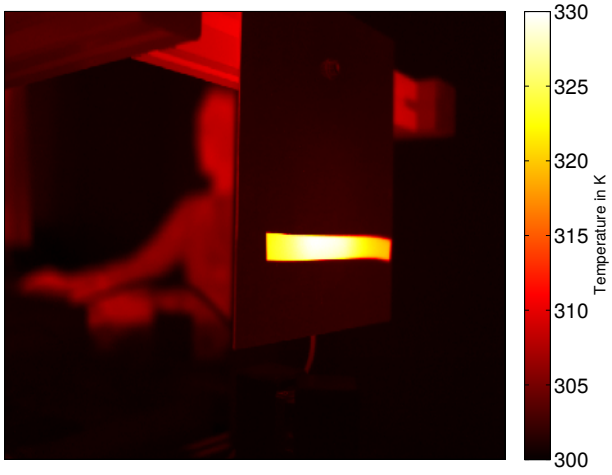

Fig. 1. Example for misinterpretation of temperature values in unknown environments: A stripe of duct tape (dielectric) sticks on a heated aluminum plate (approx. $327\ K$).

In unknown environments, there is usually no prior given emissivity information. This can lead to misinterpretations of thermal images, because, as a rule, every image pixel is assumed to have the same emissivity. In Figure 1, this is exemplarily depicted. Although the entire heated plate – including the dielectric tape – has a temperature of about $327\ K$, the measured radiation energy is very different. While the tape seems to have the highest temperature (white), the temperature of the aluminum plate is interpreted as being significantly lower (almost black). For comprehension reasons, a human silhouette, which has a temperature of about $310\ K$, can be seen in the background. The plate temperature seems to be even lower than the human body temperature.

In this work, we present an approach to prevent these misinterpretations. The key is the diverse emissivity characteristic at varying viewing angles and materials. In general, the viewing angle is the angle between the camera's optical axis and the surface normal (see Figure 2). Regarding the emissivity behavior, a distinction is made between dielectrics and metals. This circumstance is depicted in Figure 3. For dielectrics the emissivity has a constant high value at viewing angles between $0\ ^\circ$ and $50\ ^\circ$. For viewing angles above $50\ ^\circ$, emissivity decreases monotonically. The emissivity of metal surfaces, in contrast, has a constant low value at viewing angles between $0\ ^\circ$ and $60\ ^\circ$. It then grows to a maximum just before reaching a minimum at $90\ ^\circ$.

The amount of radiation energy that is measured by a TIC does not correspond to the amount of radiation energy that is emitted by the regarded surface. It is rather the sum of three radiation parts: the radiation energy emitted by the surface (subscript *obj*), the radiation energy of the surroundings reflected on the surface (subscript *amb*) and an atmospheric

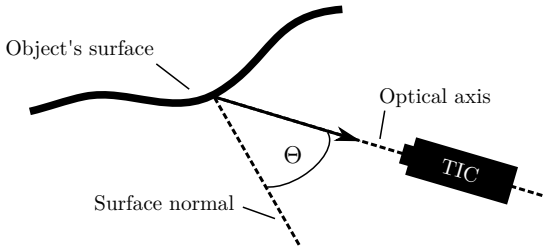

Fig. 2. Illustration of viewing angle Θ (angle between surface normal and optical axis of TIC).

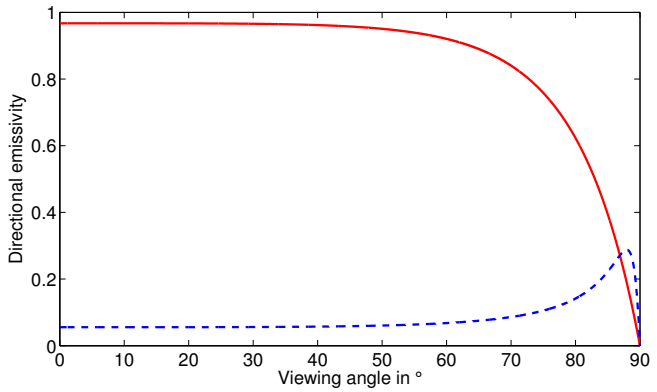

Fig. 3. Exemplary comparison of the general emissivity characteristics of dielectrics (solid line) and metals (dashed line).

part of radiation energy (subscript *atm*). This is reflected by the following equation:

$$I_{sum} = \tau\varepsilon(\Theta)I^{bb}_{obj} + \tau\left(1-\varepsilon(\Theta)\right)I^{bb}_{amb} + \left(1-\tau\right)I^{bb}_{atm}, \quad (3)$$

where I^{bb}_{obj}, I^{bb}_{amb} and I^{bb}_{atm} are black body radiation intensities of the object/surface, the ambience respectively the atmosphere. The atmospheric transmittance τ represents the influence of the medium between the regarded surface and the TIC. In our case, Equation 3 simplifies to

$$I_{sum} = \varepsilon(\Theta)I^{bb}_{obj} + \left(1-\varepsilon(\Theta)\right)I^{bb}_{amb}, \quad (4)$$

because τ is assumed to be unity which means that the medium between the surface and the camera is air.

Usual TICs do not provide output values for the detected spectral intensity. Instead, a measurement formula is used in order to interrelate the temperature with the signal that is detected by the camera. In [22], a semi-empirical adaption of Planck's law is presented:

$$S = \frac{R}{\exp\left(\frac{B}{T}\right) - F}. \quad (5)$$

This equation is camera-specific. That's why the spectral intensity I is replaced by a detector signal S of arbitrary unit. The parameters R, B and F are determined during factory calibration and can be obtained by the camera manufacturer.

IV. Explanation of the Approach

Our approach aims at improving the temperature interpretation of measurements taken by a TIC. As described in Section III, misinterpretations arise from unknown emissivities of surfaces in unexplored environments. To interpret the thermal images correctly, we consider measurements (thermal images) taken from different viewing angles making use of the emissivity's angular dependency. The general procedure is the following:

1) **Material classification:** Determination of whether the regarded surface point has the emissivity characteristic of a metal or a dielectric.
2) **Emissivity and temperature estimation:** Determination of the parameters for calculating the surface emissivity and for calculating object and ambient temperature.
3) **Image correction:** Creation of a thermal image that contains the corrected temperature values.

The following assumptions have to be made in order to use our approach:

1) The surface is assumed to be optically smooth.
2) The viewing angle Θ is known for every individual measurement.
3) The emissivity's dependency on the surface temperature is assumed to be weak.
4) The distance between the camera and the surface is small and the transmission medium is air ($\tau = 1$).
5) The surface temperature is unknown but constant ($T_{obj} = const.$).
6) The ambient temperature is unknown but constant ($T_{amb} = const.$).
7) The surface temperature is higher than the ambient temperature ($T_{obj} > T_{amb}$).

A. Material Classification

In the presented work, we want to do material classification (distinction between metal and dielectric) based on thermal images taken from different points of view. For this purpose, it is assumed that for every measurement the geometric relation between camera and surface is known. While under laboratory conditions this can be fulfilled using a geometrically calibrated experimental setup, in a real use case a 3D environment model has to be available. To determine, whether the regarded point on the surface has metal or dielectric characteristics we use the emissivity properties explained in Section III.

The emissivity characteristic can be directly transferred to the detector signal due to a linear dependency between them. This dependency becomes more clear rearranging Equation 7:

$$S = \varepsilon(\Theta)\left(\frac{R}{\exp\left(\frac{B}{T_{obj}}\right) - F} - \frac{R}{\exp\left(\frac{B}{T_{amb}}\right) - F}\right) + \frac{R}{\exp\left(\frac{B}{T_{amb}}\right) - F}. \quad (6)$$

Based on the assumptions made in Section IV the bracket term and the second addend are constant values. As a consequence, the measured detector signal is linearly dependent on the emissivity. Therefore, is it sufficient to only investigate

the behavior of the detector signal to do a basic material classification.

To perform the classification, we regard the individual pixel values in thermal images taken from different points of view and investigate their monotonicities. The procedure calculates the differences between the detector signal values of consecutive thermal images. This is done for every individual pixel in the image. To detect the emissivity characteristic of the regarded pixel, the sum of the signal differences is evaluated: If the sum is negative, we assume that the monotonicity of the measurements is decreasing. Therefore, the regarded pixel is marked as *dielectric*. Otherwise, the pixel is marked as *metal*. In the classification procedure, only viewing angles below $85\ ^\circ$ are considered. This is due to the fact that metal emissivities rapidly decrease at very high viewing angles. This would affect the monotonicity calculation. Additionally, attention must be payed when considering pixels not in the vertical line through the camera's optical axis. Due to perspective distortion, the classification for these pixels has to be done in a spatial context (with a 3D environment model).

B. Estimating Emissivity and Temperatures

The essence of this work is the estimation of the surface emissivity and temperature based on nonlinear optimization. As described in Section III, a semi-empirical equation can be used to interrelate the detected signal and the surface temperature. Combining Equations 4 and 5 – i.e. replacing the spectral intensity I with the detector signal S – leads to:

$$S = \varepsilon(\Theta)\frac{R}{\exp\left(\frac{B}{T_{obj}}\right) - F} + (1 - \varepsilon(\Theta))\frac{R}{\exp\left(\frac{B}{T_{amb}}\right) - F}. \tag{7}$$

Similar to [15], who estimate surface temperature and emissivity using the two-color method, we also create a system of nonlinear equations. These equations have the form of Equation 7. In our approach, the parameters are fitted against measurements taken from different viewing angles for individual points on the surface. To determine the most suitable parameters, least square minimization is performed in the following way:

$$\min_{\mathbf{p}} f(\mathbf{p}) = \min_{\mathbf{p}} \sum_{i=1}^{z} \left(S_i^m - S_i^c(\mathbf{p})\right)^2, \tag{8}$$

where $f(\mathbf{p})$ is the objective function and $\mathbf{p} = \{n, k, T_{obj}, T_{amb}\}$ is the set of parameters to be optimized. The signals S_i^m and S_i^c are measured/calculated values at different viewing angles (measurements at z viewing angles).

As stated before, the approach makes use of the diverse emissivity behavior according to different viewing angles, depending on whether the surface is dielectric or metal. The model used to calculate the emissivity as a function of the viewing angle refers to [21]. The model equations depend on the refractive index n and the extinction coefficient k. As stated by the authors, the model shall be used with caution in real applications. One limitation is that the model assumes "optically smooth" surfaces, which means that roughness, texture and surface imperfection have to be smaller than the wavelength of the incident radiation.

For (perfect) dielectrics, the emissivity ε_d can be calculated as:

$$\varepsilon_d(\Theta, n) = 1 - \frac{p_{d\perp}(\Theta, n) + p_{d\parallel}(\Theta, n)}{2}, \tag{9}$$

where $p_{d\perp}$ and $p_{d\parallel}$ are the polarized perpendicular and parallel parts of the specular reflectivity of the surface. Assuming that the medium between the camera and the surface is air, they can be calculated as:

$$p_{d\perp}(\Theta, n) = \left(\frac{\sqrt{n^2 - \sin^2\Theta} - \cos\Theta}{\sqrt{n^2 - \sin^2\Theta} + \cos\Theta}\right)^2 \tag{10}$$

and

$$p_{d\parallel}(\Theta, n) = \left(\frac{n^2\cos\Theta - \sqrt{n^2 - \sin^2\Theta}}{n^2\cos\Theta + \sqrt{n^2 - \sin^2\Theta}}\right)^2. \tag{11}$$

While dielectrics usually have a refractive index of $n > 1$, their extinction coefficient tends to be $k \to 0$. That's why the emissivity of dielectrics only depends on the refractive index n and the viewing angle Θ.

Metals instead have a large extinction coefficient. The equation for a metal surface emissivity according to the model is:

$$\varepsilon_m(\Theta, n, k) = \frac{\varepsilon_{m\perp}(\Theta, n, k) + \varepsilon_{m\parallel}(\Theta, n, k)}{2}, \tag{12}$$

where the perpendicular and the parallel emissivity parts are:

$$\varepsilon_{m\perp}(\Theta, n, k) = \frac{4n\cos\Theta}{\cos^2\Theta + 2n\cos\Theta + n^2 + k^2} \tag{13}$$

and

$$\varepsilon_{m\parallel}(\Theta, n, k) = \frac{4n\cos\Theta}{(n^2 + k^2)\cos^2\Theta + 2n\cos\Theta + 1}. \tag{14}$$

Varying the viewing angle and substituting the emissivity in Equation 7 with Equations 9 respectively 12 leads to a formulation that can be solved in the sense of least square minimization (Equation 8).

V. Evaluation

The approach is evaluated in three different setups: The first evaluation is performed regarding only one individual point on the surface. In the second evaluation we regard a line of pixels in the thermal images showing the benefits of the entire approach. The third evaluation is done with the camera mounted on a mobile robot using viewing angle information provided by the mapping algorithm. For all experiments a FLIR A655sc TIC with a resolution of 640 x 480 pixels is used. Working in the spectral range between $7.5\ \mu m$ and $14\ \mu m$, it has a thermal sensitivity of $30\ mK$ and a field of view of $45\ ^\circ$ x $34\ ^\circ$. Before taking measurements, the camera is intrinsically calibrated using a heated chessboard pattern. Due to the lack of any possibility to determine

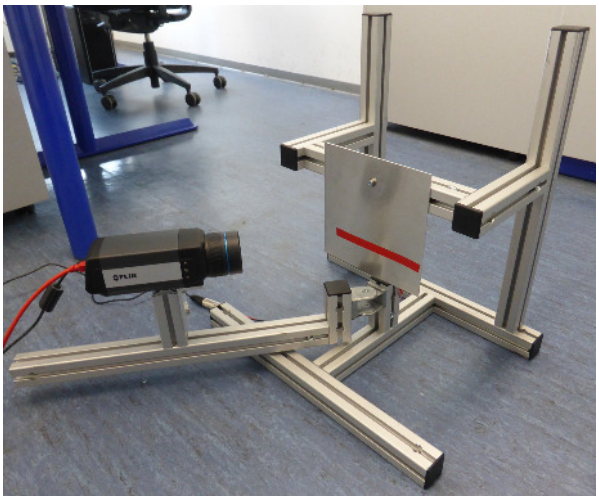

Fig. 4. Setup for experiments regarding a single point respectively a line on the surface: TIC mounted on a rotatable axis looking at a heated aluminum plate.

the real emissivities of the regarded surfaces, we limit our observations to the temperatures. These are measured using an additional thermometer. For optimization, the Nelder-Mead Simplex Method [23] is used in all evaluation setups.

A. Single Pixel Evaluation

The experimental setup is shown in Figure 4. The TIC is mounted on an aluminum profile that can be rotated around a vertical axis centered at the observed object. The regarded surface is plane and mounted exactly above the fixed rotation point. With this setup, measurements at different viewing angles can be taken. To satisfy all assumptions made in Section IV, we pay additional attention to the following details: The surface is heated with a 22 W heat pad ($T_{obj} = const.$ and $T_{obj} > T_{amb}$). The camera is mounted as closely to the surface as the focus setting allows (in our case approx. 15 cm). To simulate a constant ambient temperature, the direction of reflection is covered by a material that has a constant temperature (we solved this using a large cardboard).

In the following experiments, the point of intersection between the optical axis and the surface plane is observed. The viewing angle is altered from 10 ° to 87.5 ° (in 2.5 ° steps). At every step, the camera detector signal is recorded. The first measurements are taken looking at the dielectric tape surface of the heated plate. Figure 5 shows the results of the experiment: The solid line depicts the calculated detector signal graph based on the parameters found via least square minimization. The graph can be compared with the raw values that were taken during the measurements. See Table I for detailed values. $Err(T)$ depicts the particular absolute temperature deviation from the temperature measured by the external thermometer.

The same experiment is performed for a single point on a metal (aluminum) surface. The resulting detector signal graph is depicted in Figure 6. As for the dielectric case, the signal graph for the metal surface point shows good accordance to the raw sensor data. Merely one bigger misalignment (of about 50 units with respect to the estimated graph) at a viewing angle of 30 ° could be identified.

TABLE I. Evaluation results regarding single points on the surface.

	Dielectric point	Metal point
T_{obj_meter}	328.55 K	329.25 K
T_{obj}	330.02 K	332.29 K
$Err(T_{obj})$	1.47 K	3.04 K
T_{amb_meter}	299.55 K	298.35 K
T_{amb}	299.31 K	297.94 K
$Err(T_{amb})$	−0.24 K	−0.41 K
n	1.4349	8.3727
k	-	22.1182

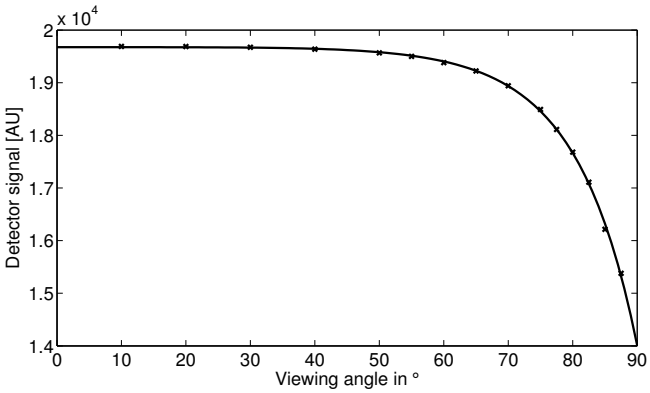

Fig. 5. Dielectric surface: detector signal graph based on estimated parameters n, T_{obj} and T_{amb} (solid line); points (x) mark measured detector signal values.

B. Pixel Line Evaluation

The following evaluation shows the benefits of the approach as a whole. As described in Section IV, image correction is performed in three steps: basic material classfication (metal/dielectric characteristic), emissivity/temperature estimation and image correction. Instead of considering single points on the surface, we now regard a line of pixels in thermal images that were taken from different viewing angles. To simplify the calculation of the true viewing angles and to ensure that the regarded surface points are the same over all measurements, the vertical line of pixels closest to the camera's optical axis is regarded (see Figure 7).

For this evaluation, two independent datasets are created. Both consist of 15 thermal images taken from viewing angles

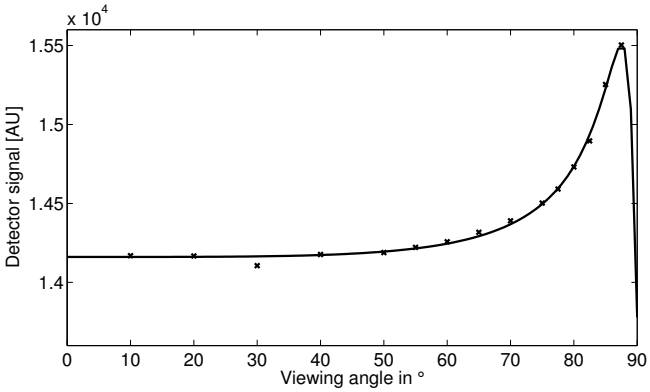

Fig. 6. Metal surface: detector signal graph based on estimated parameters n, k, T_{obj} and T_{amb} (solid line); points (x) mark measured detector signal values.

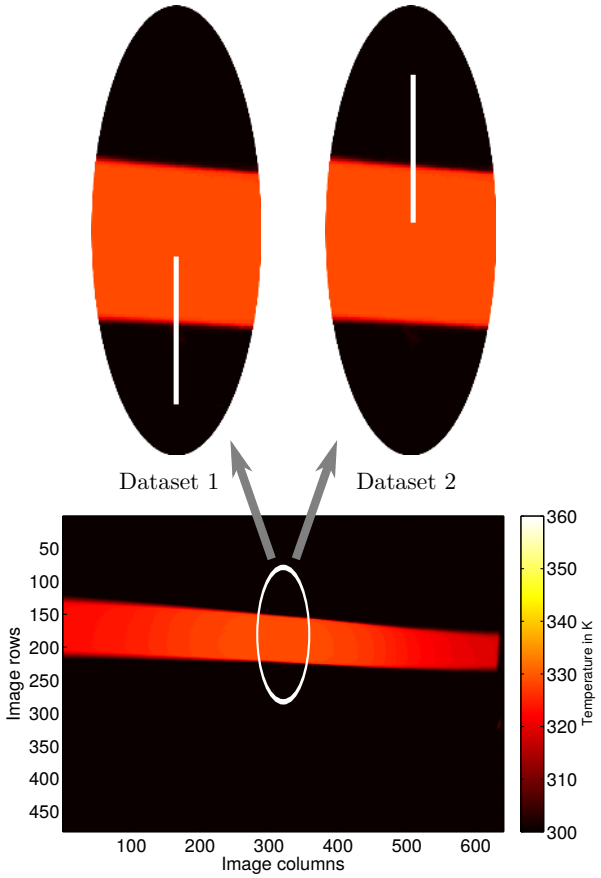

Fig. 7. Illustration of the image pixels that are considered in the two different datasets: The white lines in the pictures on the top depict the regarded pixels during evaluation. The black image areas belong to the aluminum surface (interpreted as approx. 300 K); the brighter areas belong to the dielectric tape surface (interpreted as approx. 330 K).

between 10 ° and 87.5 °. We only consider a line of pixels (100 x 1 pixels) vertically positioned to the camera's optical axis. Tracking the signal differences between consecutive images for each individual pixel allows us to classify the regarded pixel material, i.e. to decide whether the surface point follows metal or dielectric emissivity characteristics. For the two datasets the results of this classification is shown in Figures 8a and 8b.

After material classification, emissivity and temperature estimation is done as described in Section IV. For the least square minimization only the first 11 out of 15 thermal images are considered, because the estimation quality decreases if images taken at angles above 77.5 ° are used. We trace this back to inaccuracies in the experimental setup and in the measurements when taking the thermal images (e.g. caused by the construction made of aluminum profiles or errors while measuring the viewing angles). Figures 9 and 10 show the results of the final image correction. In the original image, the emissivity is assumed to be unity for each individual pixel (because there is no prior knowledge of the regarded surface). This leads to the following temperature interpretations: While the temperatures of the dielectric surface points are interpreted as $T_{obj} = 330\ K$, the temperatures of the metal points are interpreted as $T_{obj} = 300\ K$. The metal

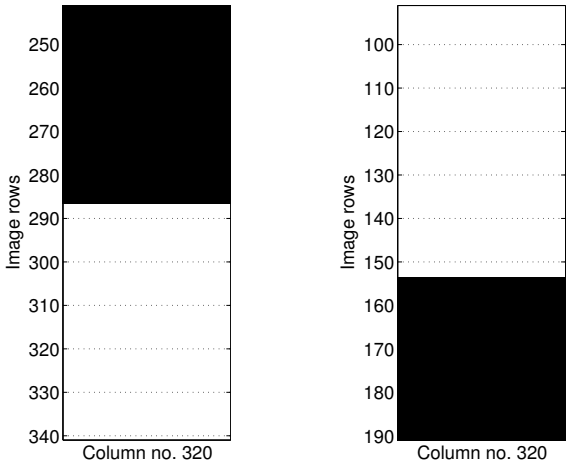

(a) Result of material classification for dataset 1.

(b) Result of material classification for dataset 2.

Fig. 8. Calculated differences between consecutive thermal images taken from different viewing angles lead to the depicted material classifications (black: dielectric tape surface, white: metal surface). See Figure 7 for an illustration of the regarded pixels.

TABLE II. Evaluation results regarding a line of points on the surface.

		Dataset 1	Dataset 2
Dielectric points	T_{obj_meter}	327.25 K	327.65 K
	T_{obj_min}	322.53 K	325.76 K
	T_{obj_max}	330.37 K	329.95 K
	T_{obj_mean}	328.39 K	329.41 K
	$Err(T_{obj})$	1.14 K	1.76 K
Metal points	T_{obj_meter}	328.35 K	328.85 K
	T_{obj_min}	322.53 K	322.53 K
	T_{obj_max}	354.62 K	354.62 K
	T_{obj_mean}	329.48 K	331.15 K
	$Err(T_{obj})$	1.13 K	2.30 K

surface points are therefore interpreted as being cooler than they actually are. After running the discussed algorithm, an improvement can be seen comparing the original with the corrected thermal images.

Although there are some outliers (see Table II), the means of the metal/dielectric points show good correspondence with the verified temperatures measured by the external thermometer. The absolute deviations $Err(T)$ from the verified temperatures are similar to the deviations calculated during the single pixel evaluation. An interesting observation is that both the minimum and maximum calculated metal temperatures are the same for the two datasets. This might be caused by running into the same local minimum during the estimation step.

C. Evaluation on a Mobile Robot

The mobile robot we use in this evaluation is a Pioneer 2 equipped with both a Kinect v2 and the FLIR camera mentioned before. We use an online temperature mapping method to additionally calculate viewing angles for each individual pixel in the image. We do not consider metal surface points in the following experiment, because the online mapping cannot be performed at large viewing angles. This is due to the Kinect's time-of-flight principle that cannot measure the depth of highly reflective surfaces. For this reason, the evaluation is performed for dielectric surface points only.

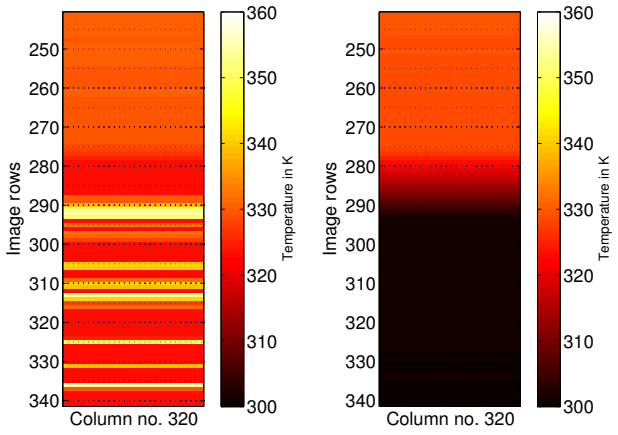

Fig. 9. Comparison of corrected (left) and original (right) thermal images for dataset 1.

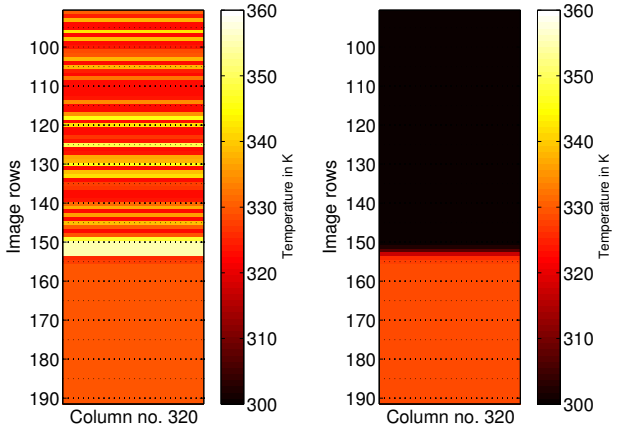

Fig. 10. Comparison of corrected (left) and original (right) thermal images for dataset 2.

Before taking measurements, intrinsic and extrinsic calibrations of the depth sensing camera and the TIC (using a heated 3D chessboard pattern) have been performed. Apart from the facts that the camera is now mounted on a mobile robot and that the estimation procedure now receives the viewing angle information directly from the surface temperature mapping algorithm (see Figures 11a and 11b), the experimental setup is the same as the one before (see Figure 12). To improve the quality of the viewing angle calculations, the dielectric surface on the heated aluminum plate is extended for this evaluation procedure.

Similar to the single pixel evaluation, we only consider one individual point on the surface in this experiment. Measurements are taken from seven different points of view. Using the algorithm, the surface temperature is estimated as $T_{obj} = 330.60\ K$; the ambient temperature as $T_{amb} = 308.67\ K$. The reference values measured by the thermometer are $T_{obj\_meter} = 327.65\ K$ respectively $T_{amb\_meter} = 301.45\ K$. This leads to absolute deviations of $Err(T_{obj}) = 2.95\ K$ respectively $Err(T_{amb}) = 7.22\ K$ referred to the verified temperature values. Although the

(a) Temperature mapping: Temperature values are projected on the 3D structure perceived by the Kinect v2 sensor.

(b) Visualization of calculated viewing angles: Dark areas represent small angles; bright areas represent large angles. Due to reflections there are some wrongly calculated angles in the metallic regions.

Fig. 11. An online temperature mapping algorithm is used to calculate viewing angles.

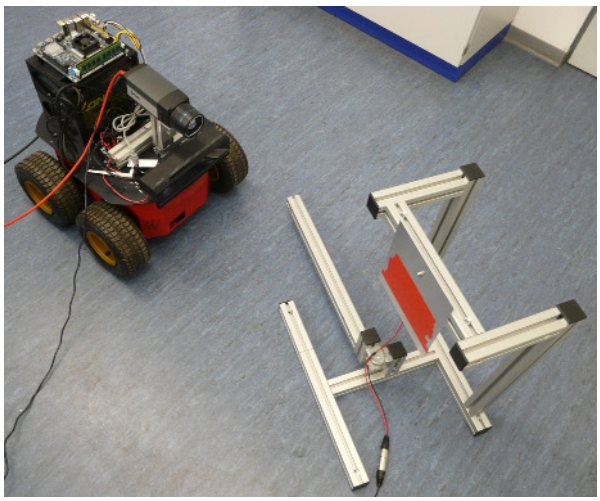

Fig. 12. Experimental setup during evaluation on the mobile robot platform: Pioneer 2 equipped with the TIC and a Kinect v2 looking at the heated dielectric surface.

estimation procedure calculates a signal detector graph that accords well to the sensor data (see Figure 13), the estimated temperatures are not as close to the verified temperatures as in the previous evaluations. Especially the large deviation of the ambient temperature shows that some additional work has to be done before our approach can be used in a real use case. However, the feasibility of emissivity/temperature estimation has been proved using the information provided by a temperature mapping algorithm.

VI. Conclusion and Future Work

The presented approach tackles the problem of misinterpretations of thermal images taken in unknown environments. These misinterpretations are caused by unknown emissivities of the regarded surface. Using the emissivity's dependency on the viewing angle, we were able to decide whether the regarded points on the surface showed dielectric or metal emissivity characteristics in order to estimate the true surface temperatures in the sense of a least square optimization. The results obtained proved the feasibility of our approach. Additionally, we evaluated the approach in combination with

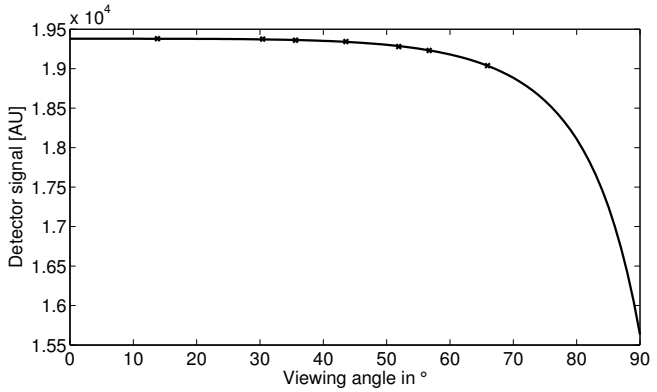

Fig. 13. Dielectric surface in the mobile robot evaluation: detector signal graph based on estimated parameters n, T_{obj} and T_{amb} (solid line); points (x) mark measured detector signal values.

a mapping algorithm that projects temperature values on a 3D model of the environment.

Regarding SAR scenarios as described in the beginning of this work, we could prove the feasibility of the presented approach implementing it on a mobile robot platform. To transfer the presented approach to an autonomously acting mobile robot, some further work has to be done. As mentioned in Section V-C, the depth sensing camera encounters difficulties providing depth information of reflective surfaces. A persistent 3D environment model could be used, so that the robot would still be able to map temperature values on the 3D structure even if he does not see the (metal) surface anymore because the viewing angle is too large. The creation of such an environment representation can be achieved using a 3D Simultaneous Localization and Mapping (SLAM) method.

Further work will also include the relaxation of the assumptions made in Section IV. Especially the assumption that the ambient temperature has to be constant will not be fulfilled in real SAR use cases. The tolerance of the estimation step towards a varying ambient temperature, i.e. reflected objects in the environment, has to be evaluated. Another topic to work on is the temperature estimation for metal surfaces, which shows some variation in the calculated values for neighboring surface points. These variations could possibly be eliminated by connecting objective functions of several surface points during optimization, i.e. by creating additional constraints in the estimation procedure.

ACKNOWLEDGMENT

This work has partly been supported within H2020-ICT by the European Commission under grant agreement number 645101 (SmokeBot).

REFERENCES

[1] R. R. Murphy, "Trial by fire [rescue robots]," *Robotics & Automation Magazine, IEEE*, vol. 11, no. 3, pp. 50–61, 2004.

[2] K. Ohno, S. Kawatsuma, T. Okada, E. Takeuchi, K. Higashi, and S. Tadokoro, "Robotic control vehicle for measuring radiation in Fukushima Daiichi Nuclear Power Plant," in *Safety, Security, and Rescue Robotics (SSRR), 2011 IEEE International Symposium on*. IEEE, 2011, pp. 38–43.

[3] B. Gernert, S. Schildt, L. Wolf, B. Zeise, P. Fritsche, B. Wagner, M. Fiosins, R. S. Manesh, and J. P. Muller, "An interdisciplinary approach to autonomous team-based exploration in disaster scenarios," in *Safety, Security, and Rescue Robotics (SSRR), 2014 IEEE International Symposium on*. IEEE, 2014, pp. 1–8.

[4] H. Mano, K. Kon, N. Sato, M. Ito, H. Mizumoto, K. Goto, R. Chatterjee, and F. Matsuno, "Treaded control system for rescue robots in indoor environment." IEEE, Feb. 2009, pp. 1836–1843.

[5] M. Zaheer Aziz and B. Mertsching, "Survivor search with autonomous UGVs using multimodal overt attention." IEEE, Jul. 2010, pp. 1–6.

[6] L. Merino, F. Caballero, J. Martínez-de Dios, J. Ferruz, and A. Ollero, "A cooperative perception system for multiple UAVs: Application to automatic detection of forest fires," *Journal of Field Robotics*, vol. 23, no. 3-4, pp. 165–184, Mar. 2006.

[7] D. W. Casbeer, R. W. Beard, T. W. McLain, S.-M. Li, and R. K. Mehra, "Forest fire monitoring with multiple small UAVs," in *American Control Conference, 2005. Proceedings of the 2005*. IEEE, 2005, pp. 3530–3535.

[8] M. Hentschel and B. Wagner, "An Adaptive Memory Model for Long-Term Navigation of Autonomous Mobile Robots," *Journal of Robotics*, vol. 2011, pp. 1–9, 2011.

[9] J. A. Sobrino, Z.-L. Li, M. P. Stoll, and F. Becker, "Multi-channel and multi-angle algorithms for estimating sea and land surface temperature with ATSR data," *International Journal of Remote Sensing*, vol. 17, no. 11, pp. 2089–2114, Jul. 1996.

[10] J. A. Sobrino and J. Cuenca, "Angular variation of thermal infrared emissivity for some natural surfaces from experimental measurements," *Applied Optics*, vol. 38, no. 18, pp. 3931–3936, 1999.

[11] E. Planas-Cuchi, J. M. Chatris, C. López, and J. Arnaldos, "Determination of flame emissivity in hydrocarbon pool fires using infrared thermography," *Fire Technology*, vol. 39, no. 3, pp. 261–273, 2003.

[12] A. Àgueda, E. Pastor, Y. Pérez, and E. Planas, "Experimental study of the emissivity of flames resulting from the combustion of forest fuels," *International Journal of Thermal Sciences*, vol. 49, no. 3, pp. 543–554, Mar. 2010.

[13] R. Usamentiaga, J. Molleda, D. F. Garcia, J. C. Granda, and J. L. Rendueles, "Temperature Measurement of Molten Pig Iron With Slag Characterization and Detection Using Infrared Computer Vision," *IEEE Transactions on Instrumentation and Measurement*, vol. 61, no. 5, pp. 1149–1159, May 2012.

[14] M. Švantner, P. Vacíková, and M. Honner, "Non-contact charge temperature measurement on industrial continuous furnaces and steel charge emissivity analysis," *Infrared Physics & Technology*, vol. 61, pp. 20–26, Nov. 2013.

[15] A. Ianiro and G. Cardone, "Measurement of surface temperature and emissivity with stereo dual-wavelength IR thermography," *Journal of Modern Optics*, vol. 57, no. 18, pp. 1708–1715, Oct. 2010.

[16] M. Litwa, "Influence of Angle of View on Temperature Measurements Using Thermovision Camera," *IEEE Sensors Journal*, vol. 10, no. 10, pp. 1552–1554, Oct. 2010.

[17] P. R. Muniz, S. P. N. Cani, and R. da S. Magalhaes, "Influence of Field of View of Thermal Imagers and Angle of View on Temperature Measurements by Infrared Thermovision," *IEEE Sensors Journal*, vol. 14, no. 3, pp. 729–733, Mar. 2014.

[18] T. Iuchi and T. Furukawa, "Some considerations for a method that simultaneously measures the temperature and emissivity of a metal in a high temperature furnace," *Review of Scientific Instruments*, vol. 75, no. 12, pp. 5326–5332, Dec. 2004.

[19] S. Vidas and P. Moghadam, "HeatWave: A handheld 3d thermography system for energy auditing," *Energy and Buildings*, vol. 66, pp. 445–460, Nov. 2013.

[20] K. Nagatani, K. Otake, and K. Yoshida, "Three-dimensional thermography mapping for mobile rescue robots," in *Field and Service Robotics*. Springer, 2014, pp. 49–63.

[21] J. R. Howell, R. Siegel, and M. P. Mengüç, *Thermal radiation heat transfer*, 5th ed. Boca Raton: CRC Press, 2011.

[22] M. Martiny, R. Schiele, M. Gritsch, A. Schulz, and S. Wittig, "In situ calibration for quantitative infrared thermography," in *QIRT*, vol. 96, 1996, pp. 3–8.

[23] J. C. Lagarias, J. A. Reeds, M. H. Wright, and P. E. Wright, "Convergence Properties of the Nelder–Mead Simplex Method in Low Dimensions," *SIAM Journal on Optimization*, vol. 9, no. 1, pp. 112–147, Jan. 1998.